

Interim Report  
for the period  
January 1988 to  
January 1989

# OH LIF Temperature Measurements in High Pressure Solid Propellant Flames

AD-A206 637

March 1989

Author:  
J. Tim Edwards

DTIC  
ELECTE  
S 5 APR 1989 D  
E<sup>a</sup>

Approved for Public Release

Distribution is unlimited. The AFAL Technical Services Office has reviewed this report, and it is releasable to the National Technical Information Service, where it will be available to the general public, including foreign nationals.

Air Force  
Astronautics  
Laboratory

Air Force Space Technology Center  
Space Division, Air Force Systems Command  
Edwards Air Force Base,  
California 93523-5000

89 4 05 083


## NOTICE

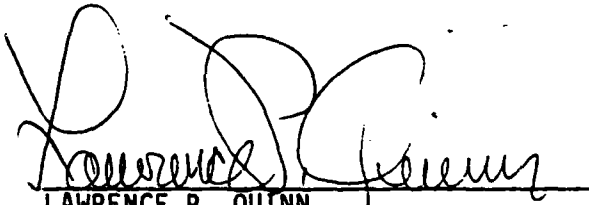
When U.S. Government drawings, specifications, or other data are used for any purpose other than a definitely related Government procurement operation, the fact that the Government may have formulated, furnished, or in any way supplied the said drawings, specifications, or other data, is not to be regarded by implication or otherwise, or in any way licensing the holder or any other person or corporation, or conveying any rights or permission to manufacture, use, or sell any patented invention that may be related thereto.

## FOREWORD


This interim report summarizes the experimental results on OH LIF Temperature Measurements to High Pressure Solid Propellant Flames in the Combustion Research Laboratory at the Air Force Astronautics Laboratory (AFAL), Edwards Air Force Base CA. The report period is from January 1988 to January 1989. The AFAL project manager was Tim Edwards.

This report has been reviewed and is approved for release and distribution in accordance with the distribution statement on the cover and on the DD Form 1473.

  
\_\_\_\_\_  
J. TIM EDWARDS  
Project Manager

  
\_\_\_\_\_  
LAWRENCE P. QUINN  
Chief, Aerothermochemistry Branch

FOR THE COMMANDER

  
\_\_\_\_\_  
ROBERT C. CORLEY  
Deputy Director, Astronautical Sciences  
Division

## REPORT DOCUMENTATION PAGE

Form Approved  
OMB No. 0704-0188

1a. REPORT SECURITY CLASSIFICATION <b>UNCLASSIFIED</b>			1b. RESTRICTIVE MARKINGS		
2a. SECURITY CLASSIFICATION AUTHORITY			3. DISTRIBUTION / AVAILABILITY OF REPORT  Approved for public release. Distribution is unlimited.		
2b. DECLASSIFICATION / DOWNGRADING SCHEDULE			5. MONITORING ORGANIZATION REPORT NUMBER(S)		
4. PERFORMING ORGANIZATION REPORT NUMBER(S)  AFAL-TR-89-003			7a. NAME OF MONITORING ORGANIZATION		
6a. NAME OF PERFORMING ORGANIZATION Air Force Astronautics Laboratory		6b. OFFICE SYMBOL (If applicable) AFAL/LSCC	7b. ADDRESS (City, State, and ZIP Code)		
6c. ADDRESS (City, State, and ZIP Code) AFAL/LSCC Edwards AFB, CA 93523-5000			9. PROCUREMENT INSTRUMENT IDENTIFICATION NUMBER		
8a. NAME OF FUNDING / SPONSORING ORGANIZATION AFOSR		8b. OFFICE SYMBOL (If applicable)	10. SOURCE OF FUNDING NUMBERS		
8c. ADDRESS (City, State, and ZIP Code)			PROGRAM ELEMENT NO. 61102F	PROJECT NO. 2308	TASK NO. M1
			WORK UNIT ACCESSION NO. E3		
11. TITLE (Include Security Classification)  OH LIF Temperature Measurements in High Pressure Solid Propellant Flames					
12. PERSONAL AUTHOR(S)  Edwards, J. Tim					
13a. TYPE OF REPORT Interim		13b. TIME COVERED FROM 88/1 TO 89/1		14. DATE OF REPORT (Year, Month, Day) March 1989	
				15. PAGE COUNT 55	
16. SUPPLEMENTARY NOTATION					
17. COSATI CODES			18. SUBJECT TERMS (Continue on reverse if necessary and identify by block number)		
FIELD	GROUP	SUB-GROUP			
21	08		Laser-Induced Fluorescence, Combustion Spectroscopy, Solid Propellant Combustion, Combustion Diagnostics. (CAW)		
19. ABSTRACT (Continue on reverse if necessary and identify by block number)  An attempt to apply OH LIF temperature measurements to high pressure solid propellant flames is described. The requirement for broadband spectral collection is discussed. In high pressure propellant flames of AP, HMX, and AN, the broadband detection decreased the light rejection of the system to the point that scattered laser light overwhelmed the OH LIF signal and rendered the measurement unsuccessful. Earlier CN and OH LIF experiments using narrowband data collection were successful, allowing radical profiles to be obtained. The difference between the two sets of experiments illustrate the need for high light rejection efficiencies in any laser-diagnostic measurement in the highly scattering environment of a propellant flame. <i>Keywords: Solid Rocket Propellants</i>					
20. DISTRIBUTION / AVAILABILITY OF ABSTRACT <input checked="" type="checkbox"/> UNCLASSIFIED/UNLIMITED <input type="checkbox"/> SAME AS RPT. <input type="checkbox"/> DTIC USERS			21. ABSTRACT SECURITY CLASSIFICATION Unclassified/Unlimited distribution		
22a. NAME OF RESPONSIBLE INDIVIDUAL Tim Edwards			22b. TELEPHONE (Include Area Code) (805) 275-5656		22c. OFFICE SYMBOL AFAL/LSCC

## TABLE OF CONTENTS

Introduction	1
Equipment and Procedures	3
Technique Application	6
Propellant Flame Experiments	26
Conclusions and Recommendations	35
References	37
Appendix A	42
Appendix B	45

Accession For	
NTIS GRA&I	<input checked="" type="checkbox"/>
DTIC TAB	<input type="checkbox"/>
Unannounced	<input type="checkbox"/>
Justification	
By _____	
Distribution/	
Availability Codes	
Dist	Avail and/or Special
<b>A-1</b>	



## LIST OF FIGURES

	Figure	Page
Figure 1.	Schematic (top view) of apparatus	5
Figure 2.	OH LIF spectrum from $R_1\ 5\ (1,0\ \text{band})$ excitation.	8
Figure 3.	OH LIF spectrum from $R_1\ 5\ (1,0\ \text{band})$ excitation.	8
Figure 4.	OH LIF schematic.	9
Figure 5.	Bandpass of "broadband" detection system.	10
Figure 6.	Bandpass shown relative to OH LIF spectrum of Figure 2.	10
Figure 7.	OH LIF excitation scan with broadband collection centered at 315 nm.	11
Figure 8.	Comparison of measured line positions of Figure 7 with literature values.	12
Figure 9.	Boltzmann-type plot of data from Figure 7, assuming saturation.	12
Figure 10.	Boltzmann-type plot of data from Figure 7, assuming non-saturation.	13
Figure 11.	Temperature fits to data from Figure 10.	13
Figure 12.	Boltzmann-type plot of data from excitation scan similar to Figure 7, except $14\ \mu\text{J/pulse}$ .	14
Figure 13.	Data of Figure 12 plotted assuming non-saturation.	14
Figure 14.	Saturation assessment.	15
Figure 15.	OH LIF spectrum, $1,0\ R_1\ 5$ excitation.	16
Figure 16.	OH LIF spectrum, $1,0\ R_1\ 2$ excitation.	16
Figure 17.	OH LIF spectrum, $1,0\ R_1\ 8$ excitation.	17
Figure 18.	OH emission spectrum.	17
Figure 19.	OH $0,0$ LIF spectrum, $0,0\ R_1\ 8+R_1\ 10$ excitation.	18
Figure 20.	OH $0,1$ LIF spectrum.	18

Figure 21.	OH 1,0 LIF spectrum.	19
Figure 22.	OH emission spectrum.	19
Figure 23.	OH emission spectrum through interference filter.	20
Figure 24.	OH LIF spectrum (1,0 R <sub>1</sub> 5 excitation) through interference filter.	20
Figure 25.	OH LIF excitation scan with broadband collection centered at 315 nm.	23
Figure 26.	Boltzmann plot of data from Figure 25.	23
Figure 27.	Effect of detection gate delay on OH LIF excitation scan temperature.	24
Figure 28.	Effect of detection gate delay on OH LIF excitation scan temperature.	24
Figure 29.	Effect of detection gate delay on OH LIF excitation scan temperature.	25
Figure 30.	Effect of 313 nm filter on OH LIF excitation scan temperature.	25
Figure 31.	Temperature sensitivity of OH R <sub>1</sub> 4 and OH R <sub>1</sub> 10 excitation.	26
Figure 32.	Schematic of OH LIF experiments in solid propellant flames.	27
Figure 33.	"OH LIF" profile in propellant flame.	29
Figure 34.	"OH LIF" profile in propellant flame.	29
Figure 35.	"OH LIF" profile in propellant flame.	30
Figure 36.	"OH LIF" profile in propellant flame.	30
Figure 37.	"OH LIF" profile in propellant flame.	31
Figure 38.	"OH LIF" profiles in propellant flame with 313 nm filter.	31
Figure 39.	"OH LIF" profiles in propellant flame with 313 nm filter.	32
Figure 40.	"OH LIF" profiles in propellant flame with 313 nm filter.	32
Figure 41.	"OH LIF" profiles in propellant flame with 313 nm filter.	33
Figure 42.	"OH LIF" profiles in propellant flames with 313 nm filter.	33
Figure 43.	"OH LIF" profiles in propellant flame with 313 nm filter.	34

Figure 44.	OH model spectrum.	46
Figure 45.	OH model spectrum.	47
Figure 46.	OH model spectrum.	47

## INTRODUCTION

It is generally believed that future improvements in the understanding of solid propellant combustion must come from a clearer picture of the chemistry and physics occurring in high pressure solid propellant flames. Condensed phase reactions also need more study. The structure and reactions of solid propellant flames are not well understood under rocket motor conditions (pressures on the order of 7 MPa (1000 psia)), although enough is known that serviceable solid propellant combustion models have been created. These models tend to emphasize the heat transfer aspects of combustion at the expense of the chemistry. This allows much useful information to be derived from the models, although many situations that are directly chemistry related, such as binder structure influences on burning behavior, are not well handled. To improve the understanding of solid propellant combustion, much more detailed information is needed on propellant flames, preferably under high pressure combustion conditions. It is important to understand the combustion chemistry since this is the type of information the propellant formulator or chemist can use to tailor and/or improve the performance of the propellant.

The temperature profile in a solid propellant flame is an important aspect of propellant combustion. Most state-of-the-art propellant combustion models (Ref. 1,2) are based upon a heat transfer analysis, with the heat released in the gas phase and condensed phase reactions being balanced against the heat needed to bring the propellant from the bulk temperature to the surface temperature plus the heat needed for any endothermic reactions such as surface pyrolysis. In such an analysis, the gas phase temperature profile would be a key piece of data, allowing calculation of the gas phase flame structure and heat release (e.g., see Ref. 3). The dependence of the temperature profile on pressure gives many clues about the flame chemistry, as well as giving an important test of any combustion model. A temperature profile would be a good test of detailed kinetic models of propellant flames now appearing (Ref. 4).

Historically, temperature profiles in propellant flames (and in the condensed phase as well) have been made with microthermocouples (Ref. 3,5,6). The thermocouple beads (often  $< 10\text{ }\mu\text{m}$ ) are imbedded into the propellant. As the propellant burns down past the thermocouple, the temperature profile is obtained. Thermocouple temperature measurements have several advantages and disadvantages. Among the advantages are the relatively simple (inexpensive!) experimental apparatus needed and the ability to measure the temperature in both the condensed and gas phases. Among the disadvantages are the relatively limited temperature range ( $T_{\text{max}} \sim 2000\text{ K}$ ), the possibility of perturbing the flame since the thermocouple is an intrusive probe, and the possible problems of the thermocouple response time and correction for heat loss. The environment of a solid propellant flame is a very difficult one, with temperature changes of  $\sim 10^4\text{ K/s}$  occurring near the surface. It is this problem of thermocouple response time (resolution) that leads to an interest in laser-based combustion diagnostics for temperature measurements. These techniques are, of course, limited to the gas phase, although a similar technique has been developed for surface temperature measurements (Ref. 7).

Laser-based combustion diagnostics such as coherent anti-Stokes Raman scattering (CARS) and laser-induced fluorescence (LIF) are often used to make temperature measurements in flames (Ref. 8). CARS can be used to measure the temperature of major flame species such as CO and  $\text{N}_2$ , while LIF is used to measure the temperature of radicals such as CN and OH. Seeding



atomic species into flames to make temperature measurements using LIF is also common (Ref. 9,10) (this type of seeding would be relatively easy in a solid propellant flame). The LIF rotational temperature obtained by these techniques is that of the ground electronic state of the molecule, which is generally equal to the translational temperature of the flame. Thus LIF temperatures do not yield the high excitation temperatures calculated from emission (chemiluminescence) spectra (Ref. 11,12), which can be well above the adiabatic flame temperature. This report describes an attempt to apply OH LIF temperature measurements to high pressure solid propellant flames. Successful OH LIF temperature measurements have been made in atmospheric pressure propellant flames (Ref. 13). Successful CARS temperature measurements on high pressure propellant flames have recently been reported (Ref. 14). Other spectroscopic methods have been used to measure propellant flame temperatures, such as sodium line-reversal (Ref. 15) and infrared emission (Ref. 16). The main limitation of these techniques is that the temperature obtained is a line-of-sight average of emission and thus only moderate spatial and temporal resolution is obtained. In general, then, only thermocouples have generated useable temperature measurements in solid propellant flames until recently.

LIF measurements in solid propellant flames are generally difficult because of the optical thickness of the propellant flames (Ref. 12,18). The scattering from the particles in the flames is of much higher intensity than LIF at the same or nearby wavelengths, so resonance fluorescence (LIF collected at the excitation wavelength) experiments are essentially impossible. Exciting and collecting the fluorescence in different bands of a molecule is the usual solution for this problem. For example, one could excite CN LIF in the 0,1 band and observe LIF in the 0,0 band (Ref. 12,18). The OH LIF temperature measurements described in this paper were performed by exciting LIF in the OH 1,0 band at ~281 nm and observing the resulting LIF in the OH 1,1 band from 312-320 nm. Filters can also be used to aid in rejection of unwanted scattered light at the laser wavelength. The particles that cause the scattering can also cause severe beam attenuation (Ref. 12,18). With certain propellants, this can occur at relatively low pressures (1-5 atm).

## EQUIPMENT AND PROCEDURES

The solid propellant flames were studied by burning propellant strands in a nitrogen-purged, high pressure combustor (Ref. 17). This combustor is a variant of the standard "window bomb" or "strand burner" in widespread use in solid propellant combustion studies. Optical access is provided by eight 3.8-cm diameter, 2-cm thick sapphire windows distributed at 45 degree intervals around the combustor. The diagnostic laser intensity (and presumably any LIF signals generated) was reduced 20% in passing through one of the windows. For laser-diagnostic purposes, a means to keep the burning propellant surface at a constant level is often desirable. This is accomplished by a servo mechanism which elevates the surface of the solid propellant as it burns down, thus keeping the surface at a constant level relative to the collection volume of the detection systems. The servo system employs a 100 mW HeNe laser passing across the propellant surface, with a feedback-control system elevating the propellant strand to keep the fraction of the beam blocked by the surface constant (Ref. 17). In general, the system works fairly well at pressures below 2 MPa (300 psia), depending on the propellant, but the increases in flame optical thickness and propellant burn rate that accompany increases in pressure cause the system to work poorly at higher pressures. An alternative is to allow the propellant to burn down through the collection volume, in essence collecting sequential data at increasing distances above the propellant surface. All experiments were run under nitrogen. The propellant was burned in strands of about 3-4 cm in length and 6 mm in diameter, with the sides of the propellant coated with a thin layer of a fluorocarbon grease as an inhibitor. Depending on the pressure, these strands burned from 1 to 20 seconds. The short burn time of the strands did not permit spectral scanning; the detection system was based on the need for rapid data collection. A premixed flame source constructed from 6 mm tubing could be placed in the combustor in place of the strand for tuning of the lasers and alignment of the detection systems. The flame was usually run with a  $\text{N}_2\text{O}/\text{CH}_4$  (molar) ratio of approximately 2. Several propellants were examined: HMX1 (70% HMX, 17% TMETN, 13% polyester binder), HMX2 (80% HMX, 20% polyester binder), AP1 (87% AP, 13% polybutadiene binder), and AN1 (72% AN, 12% TMETN, 16% glycidyl azide polymer binder). The propellant burn rates were HMX1, 1.4 mm/s at 1.5 MPa (200 psig); HMX2, 0.8 mm/s at 1.5 MPa (200 psig); AP1, 2.4 mm/s at 0.5 MPa (50 psig); and AN1, 1.7 mm/s at 0.8 MPa (100 psig). For more information (see Ref. 12,18).

The OH LIF experiments were performed by pumping a Lambda-Physik FL 2002 dye laser with 308 nm light from a Lambda-Physik EMG 201 MSC excimer laser. The laser system had a maximum repetition rate of 80 Hz. The dye laser was operated with Lambdachrome LC 5400 dye (Coumarin 153), with a nominal bandwidth of  $0.1\text{ cm}^{-1}$  after frequency doubling and a pulse width of 25 ns. The beam was focussed into the propellant flame with a 10-cm focal length fused silica lens. The resulting focal volume diameter was approximately  $50\text{ }\mu\text{m}$ . The short focal length lens minimized damage to the sapphire windows. After passing through the combustor windows, a small portion of the beam passed onto a photomultiplier tube for monitoring beam transmission through the combustor and propellant flame. The laser power was also measured before the combustor with a photo-multiplier tube to monitor laser pulse energy levels. This is illustrated in Figure 1. In experiments where the laser was scanned, the laser wavelength changed in  $0.0004\text{ nm}$  steps, with the wavelength held at each particular value for 0.33 sec. Thus a scan over 0.2 nm required approximately ten minutes. In these initial experiments, the data collection was not synchronized with the laser scanning mechanism, so data collection occurred while the laser

wavelength was changing. This affected relatively few data points so that the lack of synchronization wasn't a problem in these experiments. In future experiments, the scanning and data collection will be synchronized.

The LIF signals were collected at 90 degrees from the laser beam, collimated, and focussed onto a spectrometer entrance slit with 1:1 magnification using two 10 cm focal length fused silica lenses. The image was rotated 90 degrees with a mirror assembly such that the vertical spectrometer entrance slits were projected horizontally onto the propellant flame. The photomultiplier tube (PMT) detection system employed a RCA C31034A tube attached to a Spex 1870 1/2 meter monochromator (1200 and 300 grooves/mm gratings,  $\sim 1.5$  and 6 nm/mm dispersion). The collected LIF signals were focussed onto the slit of the monochromator, with the vertical resolution of the system in the flame thus being the entrance slit width (typically 20-50  $\mu\text{m}$ ). The slit height, and thus the width of the collection volume along the path of the laser beam, was typically 2 mm. In earlier LIF experiments (Ref 12,18), it was often found necessary to add a narrowband ( $\sim 10$  nm bandwidth) filter to aid in the separation of the LIF signals and the scattered laser light in the propellant flames. The PMT signal was processed by a Stanford Research Systems SR250 gated integrator, along with the laser pulse energy and transmission signals. The data collection was controlled by an Apple Macintosh computer through a Stanford Research Systems SR245 computer interface. Post processing was accomplished on a Macintosh computer using Kaleidagraph software. Propellant experiments were usually performed by setting the spectrometer on the desired wavelength and monitoring the LIF signal as a function of time, as the propellant burned down through the collection volume, thus single-pulse data acquisition and high laser repetition rates were desirable to resolve the propellant flame structure as finely as possible.

Some OH emission results are also mentioned in this report for comparison purposes. In these experiments, detection was performed with an EG&G/PAR 1420 Reticon diode array (700 elements) attached to a Spex 1877 Triplemate spectrometer. The Reticon was controlled by an EG&G/PAR OMA II 1215/1218 detector controller and data acquisition system. The Triplemate is a triple spectrometer with an initial "filter" stage which allows high light rejection (Ref. 12,18). Three turret-mounted gratings were available, with the highest resolution grating being a 2400-gr/mm grating with a dispersion of 0.0175 nm/pixel. The Reticon was used extensively in studies of solid propellant flame chemiluminescence, where accurate background measurements were imperative due to the presence of a strong continuous background, resulting from CO+O chemiluminescence or emitting particles. The sensitivity of the Reticon was usually too low for single-pulse LIF experiments (Ref. 12,18).

The 0.5-m spectrometer/PMT system has several difficulties in operation in propellant flames. Heavily particulate laden flames cause Mie scattering (or laser-modulated particulate incandescence (Ref. 19) or rotational Raman (Ref. 8)) interference with the LIF signals, even with a filter in the optical system. Obviously, the lack of a simultaneous measurement of a non-resonant wavelength as a background correction is a real limitation in this type of system. Separate experiments were performed with either the laser or spectrometer detuned from resonance to assess the contribution of the non-resonant scattering to the desired LIF signals (Ref. 12,18). Additionally, the optical thickness of the propellant flames increases dramatically with pressure (higher soot density?), so higher pressure measurements are doubly difficult (Ref 12,17,18). However, for several propellants with relatively non-sooting flames, unambiguous CN and OH

LIF signals were obtained up to pressures of 3.5 MPa using this system. For very sooty propellants such as AN1, the desired signal was difficult to obtain under most circumstances. The origin of the soot is probably found in the fuel-rich stoichiometry of the solid propellants. In studies on a wide variety of hydrocarbons, Glassman found  $\phi_c$ 's (critical equivalence ratios above which a flame produced soot) of  $1 \pm 0.2$  at flame temperatures of 1800-2400 K (Ref. 46). The stoichiometric equivalence ratio was based on CO and H<sub>2</sub>O. It was also found that (1) the tendency to soot increased ( $\phi_c$  decreased) for a given stoichiometry as the temperature decreased, (2)  $\phi_c$  decreased as the "number of carbon-carbon bonds" in the fuel molecule increased, and (3) diffusion flames and premixed flames show different sooting behavior for a given fuel. Using a modification of Jain's method of calculating propellant stoichiometries (Ref. 47) to account for a definition of stoichiometric based on CO and H<sub>2</sub>O, the stoichiometries of the propellants in this paper were calculated as  $\phi_e = 1.23, 1.46, 0.95$ , and  $0.90$  for HMX1, HMX2, AP1, and AN1, respectively.  $\phi > 1$  implies fuel-rich stoichiometry,  $\phi = 1$  implies stoichiometric (CO and H<sub>2</sub>O), and  $\phi < 1$  implies oxidizer-rich stoichiometry. All the propellants are within the range of stoichiometries at which flames have been found to soot, and the lower temperature of the AN1 flame would help explain the increased sooting tendency of this flame (as evidenced by the optical thickness of the flame) compared to the AP flame. If the sooting tendency of propellant flames could be related to the fuel decomposition mechanisms (as has been done for hydrocarbons (Ref. 46)), some interesting results would undoubtedly emerge. For laser-diagnostic purposes, however, the soot is a large hindrance to obtaining species and temperature data.

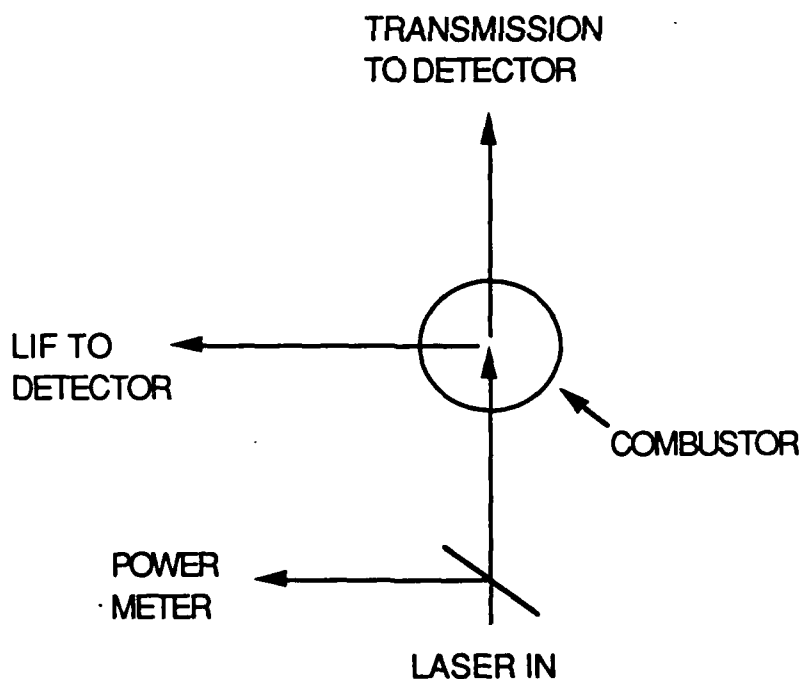


Figure 1. Schematic (top-view) of apparatus.

## TECHNIQUE APPLICATION

OH is found in all flames containing hydrogen and oxygen and is often found in high concentrations. For example, the equilibrium mole fraction of OH in a stoichiometric  $\text{CH}_4/\text{N}_2\text{O}$  (1:4) flame at 1 atm is 0.04. For comparison, the equilibrium OH mole fractions and adiabatic flame temperatures (K) of the four propellants at 3.5 MPa (500 psig) are 0.0142/2970 (AP1), 0.00066/2620 (HMX1),  $8 \times 10^{-8}$ /2050 (HMX2), and 0.0001/2140 (AN1). The equilibrium OH concentration is not the absolute concentration expected, but is an indication of the relative stoichiometries in the various flames. In addition to occurring at high concentration, OH is a good temperature probe since it is usually distributed throughout a flame (Ref. 20,21). This was also found to be the case in several propellant flames (Ref. 12). In contrast, radicals such as CN and NH are confined to certain propellant reaction zones, typically very near the surface, and thus are not as versatile as OH as a temperature probe. Finally, OH is probably the best understood radical in a flame environment, with many studies made of the spectroscopy and laser-excitation dynamics of OH (e.g., Ref. 22-37). For certain propellants (notably double-base propellants and low-energy nitramine propellants which have "dark" zones where one would expect little OH) and certain temperature regimes (low temperatures especially), OH is probably not the best molecule for LIF studies. A good possibility for these propellants and conditions is NO. The possibility of using NO LIF as a temperature probe in propellant flames is under investigation at NWC. NO has been used as a flame thermometer (e.g., Ref. 38). NO has several unique problems, notably the high concentrations found in propellant flames, causing beam attenuation/absorption problems, and the relative (compared to OH) lack of spectroscopic information.

OH LIF measurements are performed by exciting transitions in the OH  $A^2\Sigma-X^2\Pi$  system (Ref. 39). For applications where the separation of the desired fluorescence from scattered laser light is difficult, such as 2-D imaging (Ref. 13,40) or propellant flame probing (Ref. 13,18), the LIF excitation and detection are performed in different bands separated by 20-30 nm. For example, the measurement might be excite 0,1-detect 0,0 or excite 1,0-detect 1,1. The spectral separation of the bands enhances the separation of the desired LIF from the undesired scattering at the laser wavelength. For these experiments, the second measurement method (excite 1,0-detect 1,1) is used. For example, the LIF spectra obtained in the outer cone of the 1 atm 1:2  $\text{CH}_4/\text{N}_2\text{O}$  calibration flame from the excitation of the  $R_1$  5 line of the OH 1,0 band are shown in Figures 2 (0,0 and 1,1 band) and 3 (1,0 band). A schematic of the LIF is shown in Figure 4. In the case where no rotational redistribution occurs in the laser-populated upper state, the only lines present in the spectra would be the  $R_1$  5,  $Q_1$  6, and  $P_1$  7 lines in the 1,0 and 1,1 bands (ignoring weak satellite transitions). As can be seen in Figures 2 and 3, considerable rotational redistribution has occurred in the upper state prior to the molecule radiating. Vibrational redistribution has also occurred, as shown by the presence of 0,0 band LIF. The excite 1,0-detect 1,1 scheme has the added advantage of minimizing the self-absorption problems that occur when the 0,0 band is involved (Ref. 34,36).

This rotational redistribution makes calculations of OH concentration more complicated. In a well-characterized flame environment, detailed calculations involving the dynamics of the LIF have been made (Ref. 8). Saturating the OH LIF simplifies these calculations (Ref. 8). For temperature measurements, detailed calculations are typically avoided by using broadband collection; for example, collecting all the fluorescence from the 1,1 band in Figure 2. A bandpass

of ~20 nm is required (Ref. 28). This was obtained in our experiments by replacing the 1200-gr/mm grating used in earlier LIF work (Ref. 12,18) with a 300-gr/mm grating, which gave a bandpass of ~20 nm when the rear slit of the spectrometer was opened to 3 mm. This is shown in Figure 5, where the bandpass is measured by scanning the spectrometer over the laser line. The bandpass was centered at 315 nm for the OH LIF temperature measurements, as illustrated in Figure 6. Temperatures are obtained in this type of experiment by scanning the laser across many rotational lines in the linear or saturated fluorescence regime and collecting the resulting fluorescence (an "excitation" scan (Ref. 8)). The collected fluorescence is proportional to the ground state population of the given transition, the absorption coefficient (transition probability), and the degeneracy of the ground state rotational level. If one assumes a Boltzmann distribution (rotational population proportional to  $\exp(-\text{rotational energy}/kT)$ ), then the temperature can be found. Thus,  $I_{\Omega} \sim g''B(v,J)\exp(-hcE_r/kT)$ , where  $I_{\Omega}$  is the fluorescent intensity,  $g''$  is the degeneracy of the ground state rotational level ( $g''=2J''+1$ ),  $B(v,J)$  is the Einstein coefficient for absorption (Ref. 41), and  $E_r$  is the rotational energy of the ground state rotational level (found from tables (Ref. 39,48) or approximated as  $\sim B_v J''(J''+1)$  (ref. 8)). The data used are listed in Appendix 1. Thus a plot of  $\ln I_{\Omega}/g''B(v,J)$  vs  $E_r$  will have a slope of  $-hc/kT$ . These equations are valid for the linear fluorescence regime, where LIF signal is proportional to laser power. Under saturation conditions, the equations change somewhat (Ref. 35), with  $-hc/kT$  being the slope of a plot of  $\ln [I_{\Omega}(1/g''+1/g')]$  vs  $E_r$ .

An example of an excitation scan is shown in Figure 7. Assignment of lines was simple and accurate, as shown in Figure 8. The estimated spectral irradiance for the experiment of Figure 7 is approximately  $8 \times 10^6 \text{ W/cm}^2\text{-cm}^{-1}$ , much larger than the saturation estimate of  $1 \times 10^6 \text{ W/cm}^2\text{-cm}^{-1}$  for atmospheric pressure flames (Ref. 8). The irradiance was calculated using a bandwidth of  $0.1 \text{ cm}^{-1}$  (dye laser before frequency doubling is  $0.2 \text{ cm}^{-1}$ ), a pulse duration of 25 ns, and a focussed beam diameter of 50  $\mu\text{m}$ . The focussed beam diameter was estimated as  $d=f\Theta$ , with  $f$  (lens focal length)=10 cm and  $\Theta$  (beam divergence)=0.5 mrad. When the data was reduced as described assuming complete saturation, it was found that the various branches did not fall on a single line. This is shown for the excitation scan of Figure 7 in Figure 9, yielding best fit temperatures of 2930, 1584, and 2638 K for the  $R_1$ ,  $R_1'$ , and  $R_2$  branches. If the same data is reduced by assuming non-saturation, a similar type of Boltzmann plot is obtained; as shown in Figure 10, best fit temperatures of 2373, 3560, and 2288 K are obtained for the  $R_1$ ,  $R_1'$ , and  $R_2$  branches. In both cases, the main branches ( $R_1$  and  $R_2$ ) fall on essentially the same curve (as shown in Figure 10), while the satellite  $R_1'$  branch gives a substantially different temperature. A consistent exception to this linear behavior was seen for those lines with low quantum numbers, such as  $R_1$  1 and  $R_1$  2, which were ignored in the temperature fits discussed above. Non-linearity of Boltzmann plots at low rotational energy is relatively common (e.g., Ref. 49).

When a similar experiment was performed with a higher laser energy (14  $\mu\text{J/pulse}$ ), the results shown in Figures 12 and 13 were obtained. The OH LIF temperatures calculated were 2763, 1535, and 2534 K (saturated assumption) and 1905, 3695, and 1954 K (non-saturated assumption) for the  $R_1$ ,  $R_1'$ , and  $R_2$  branches. It is apparent that the OH LIF is still partially saturated, even with the substantially higher laser energy. In fact, saturation was not evident in an

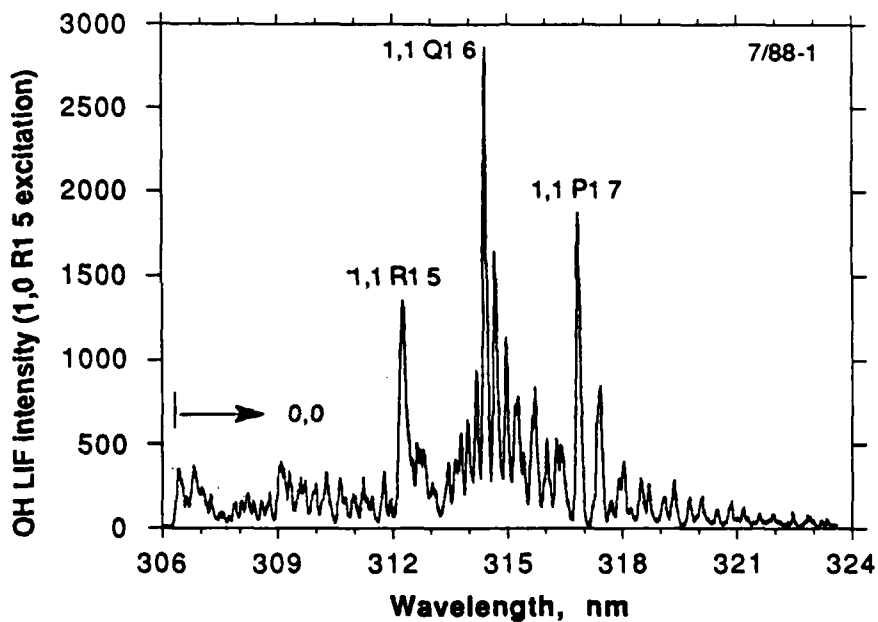


Figure 2. OH LIF spectrum from R<sub>1.5</sub> (1.0 band) excitation. CH<sub>4</sub>/N<sub>2</sub>O flame, 1 atm (air), outer cone, 0.3 mJ/pulse in flame, 30  $\mu$ m slits, 1200-gr/mm grating.

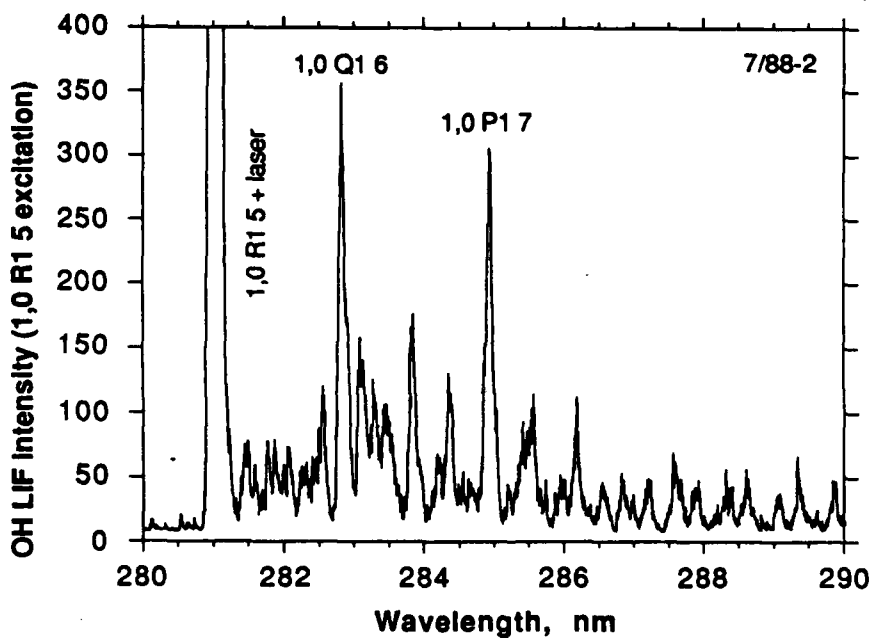


Figure 3. OH LIF spectrum from R<sub>1.5</sub> (1.0 band) excitation. CH<sub>4</sub>/N<sub>2</sub>O flame, 1 atm (air), outer cone, 0.3 mJ/pulse in flame, 30  $\mu$ m slits, 1200-gr/mm grating.

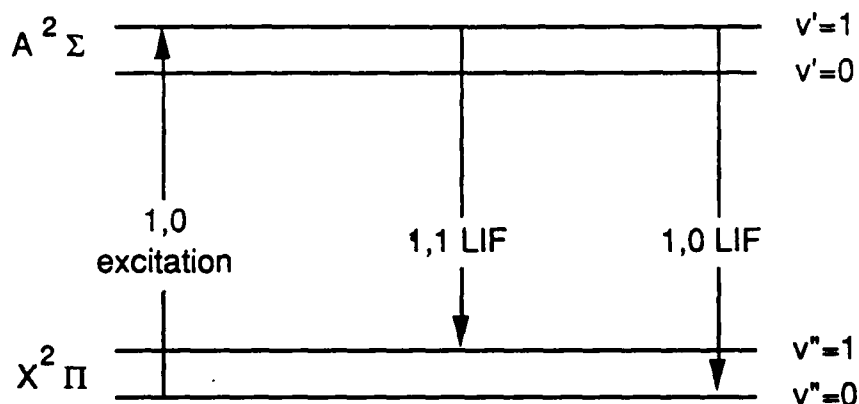


Figure 4. OH LIF schematic.

LIF-vs-laser power plot until laser powers on the order of  $100 \mu\text{J/pulse}$  was reached, as shown in Figure 14. One possible reason that the experimental data is partially saturated, even though the irradiance is greater than the saturation estimate, is that saturation is sensitive to the detection gate used (both width and delay) and other parameters such as inclusion of the "wings" of the laser beam (Ref. 8,35). Using a method for reducing partially saturated data (Ref. 45), the temperature for the excitation scan of Figure 7 is  $2600 \pm 80 \text{ K}$ , with the  $R_1$ ,  $R_1'$  and  $R_2$  branches falling on the same curve (calculation performed by Steve Zabarnick, UDRI). The adiabatic flame temperature of the calibration flame is  $2500 \pm 400 \text{ K}$  (the uncertainty is due to uncertainty in the gas flow rates and the flame stoichiometry). Thus, the corrected temperature is apparently reasonable. This data may be compared with that of Anderson, et al (Ref. 22), where all branches appeared to fit on one line in an  $\ln I_{\text{fl}}/g''B(v,J)$  vs  $E_r$  plot (in an excite 1,1-detect 1,1 experiment), thus indicating non-saturation. The spectral irradiance was approximately  $3 \times 10^6 \text{ W/cm}^2\text{-cm}^{-1}$  ( $1 \mu\text{s}$  pulse,  $0.34 \text{ cm}^{-1}$  bandwidth,  $200 \mu\text{m}$  beam focussed diameter,  $0.3 \text{ mJ/pulse}$ ,  $11.4\text{-cm}$  focal length focussing lens). This discussion indicates the importance of saturation corrections in obtaining accurate OH LIF temperature measurements, especially when the satellite bands are used.

Although the calibration flame used in these experiments was not the well-characterized flame needed for detailed spectroscopy studies, it appeared valuable to undertake some background experiments to examine the effect of various parameters, such as gate width and timing, on LIF temperature measurements. It is anticipated that detailed studies will be performed in the high pressure flame facility under construction in this laboratory. In addition, the effect of a narrowband filter (Oriel 56510,  $313 \text{ nm}$  center bandpass,  $11\text{-nm}$  FWHM bandwidth, 25% peak transmission) on the temperature measurements was examined for use during the propellant flame OH LIF temperature measurements.



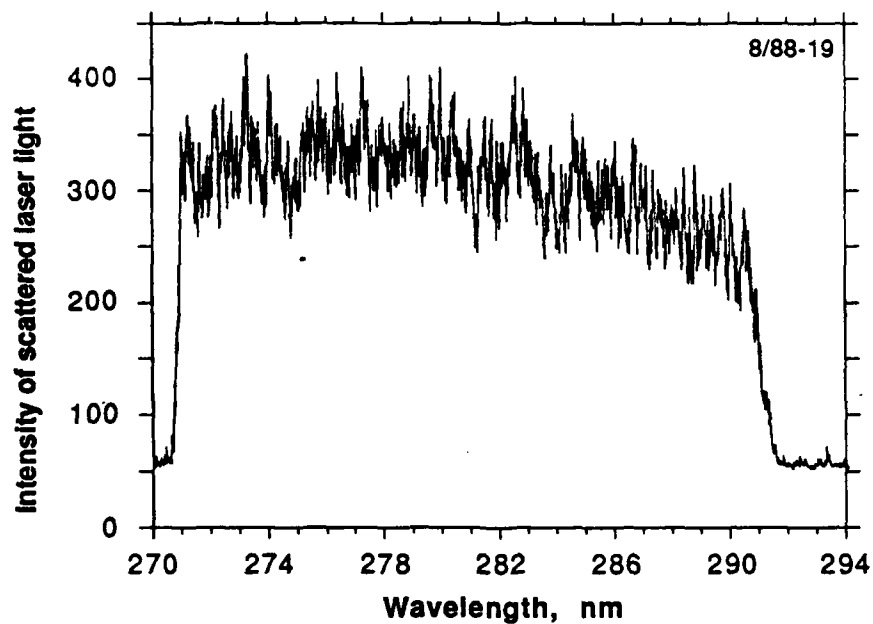


Figure 5. Bandpass of "broadband" detection system. Measured by scanning spectrometer over laser line (281.13 nm), 300 gr/mm grating, 50- $\mu$ m/3-mm slits, no flame.

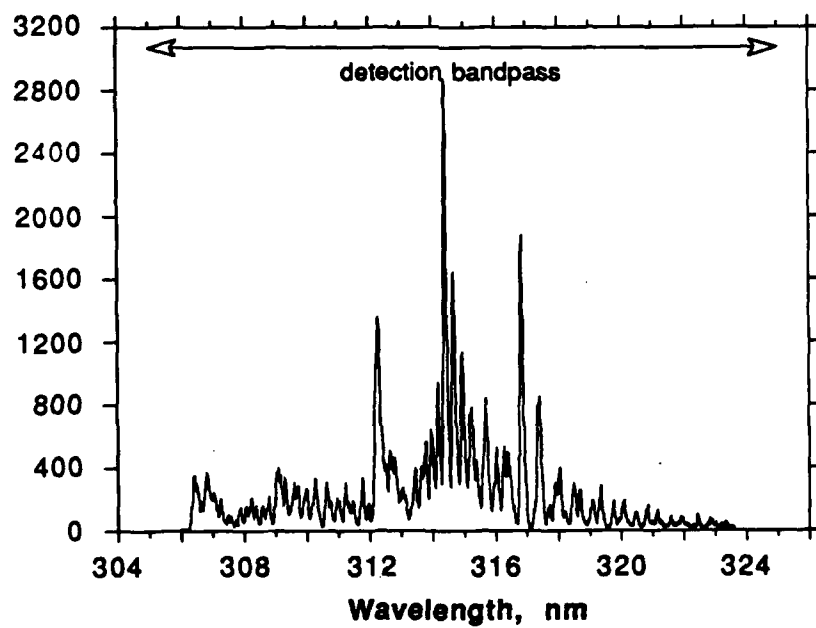


Figure 6. Bandpass shown relative to OH LIF spectrum of Figure 2 (for spectrometer set to 315 nm).

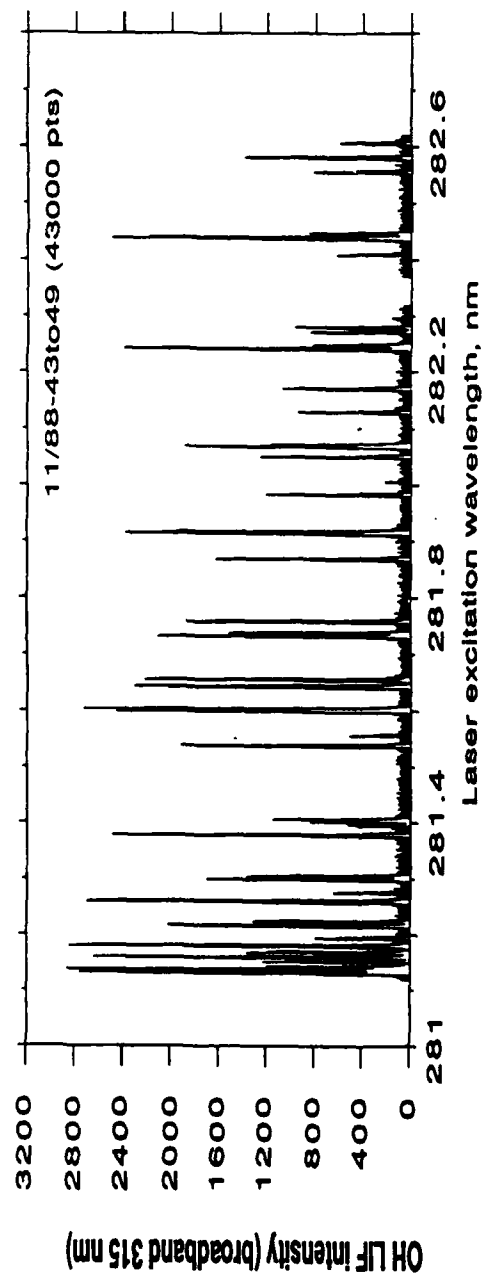


Figure 7. OH LIF excitation scan with broadband collection centered at 315 nm.  $\text{CH}_4/\text{N}_2\text{O}$  flame, 1 atm (air), outer cone, 0.4  $\mu\text{J}/\text{pulse}$  in flame, 10 Hz, 3 pulse average, 30  $\mu\text{m}/3$  mm slits, 300 gr/mm grating, 43000 data points.

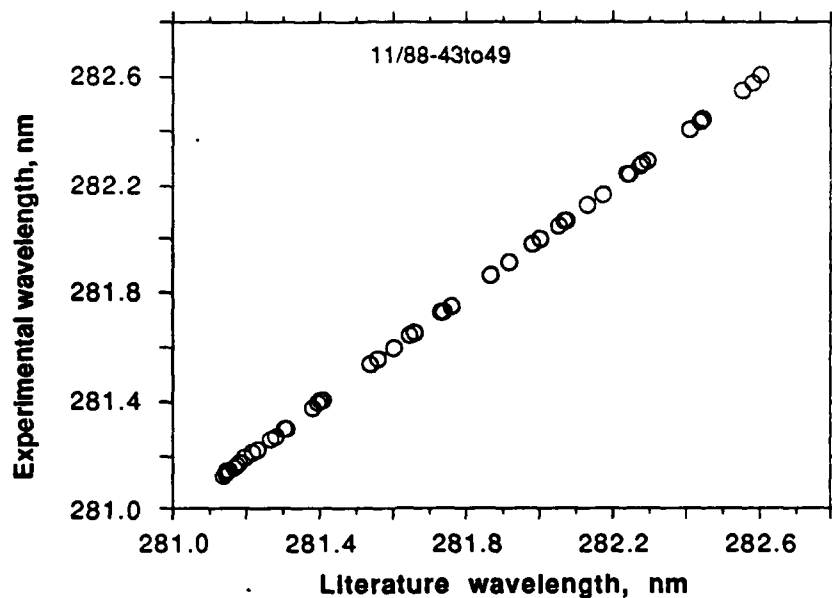


Figure 8. Comparison of measured line positions of Figure 7 with literature values (Ref. 39).

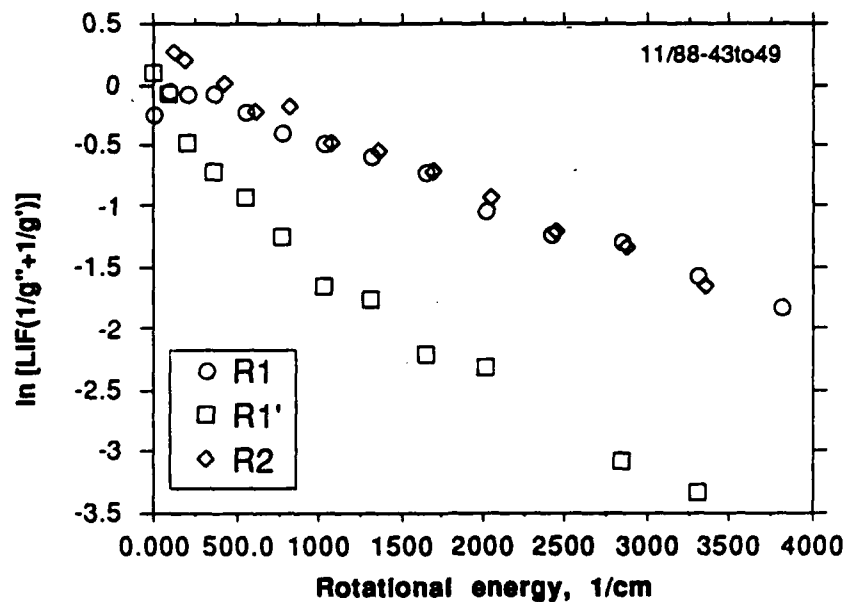


Figure 9. Boltzmann-type of plot of data from Figure 7, assuming saturation.

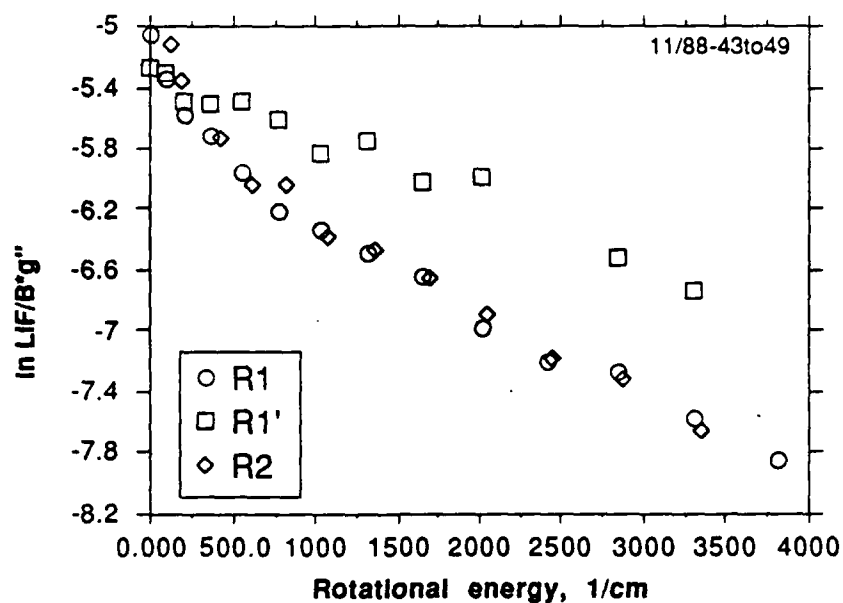


Figure 10. Boltzmann-type plot of data from Figure 7, assuming non-saturation.

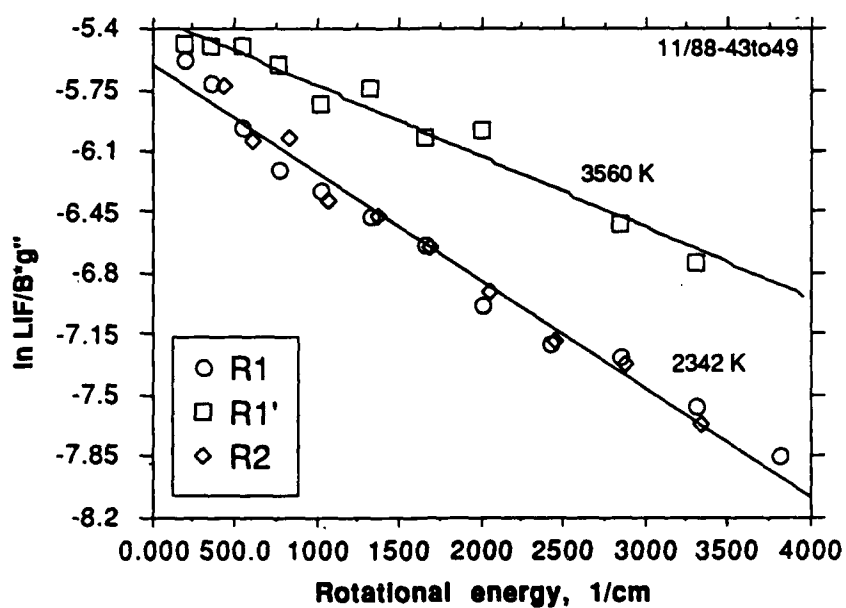


Figure 11. Temperature fits to data from Figure 10. Data with  $N''=1,2$  eliminated.

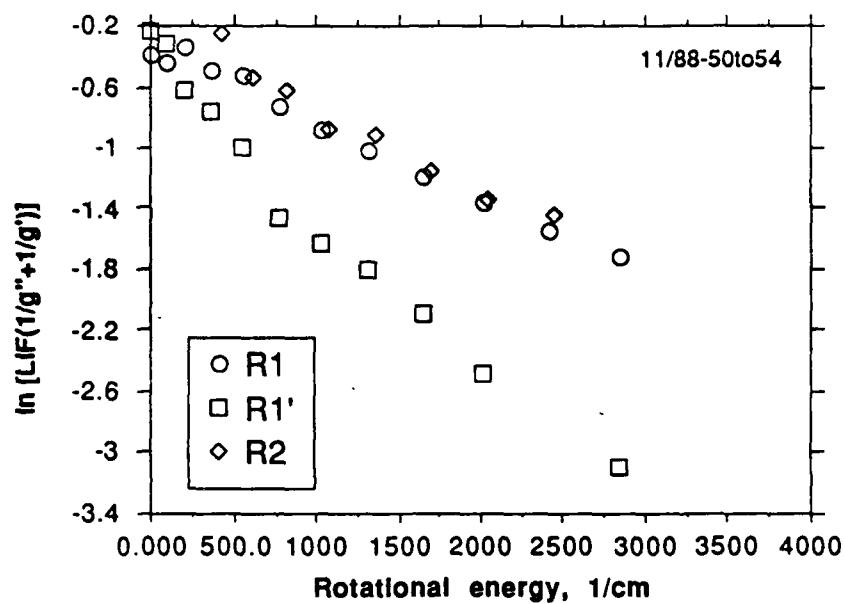


Figure 12. Boltzmann-type plot of data from excitation scan similar to Figure 7, except 14  $\mu J/pulse$ .

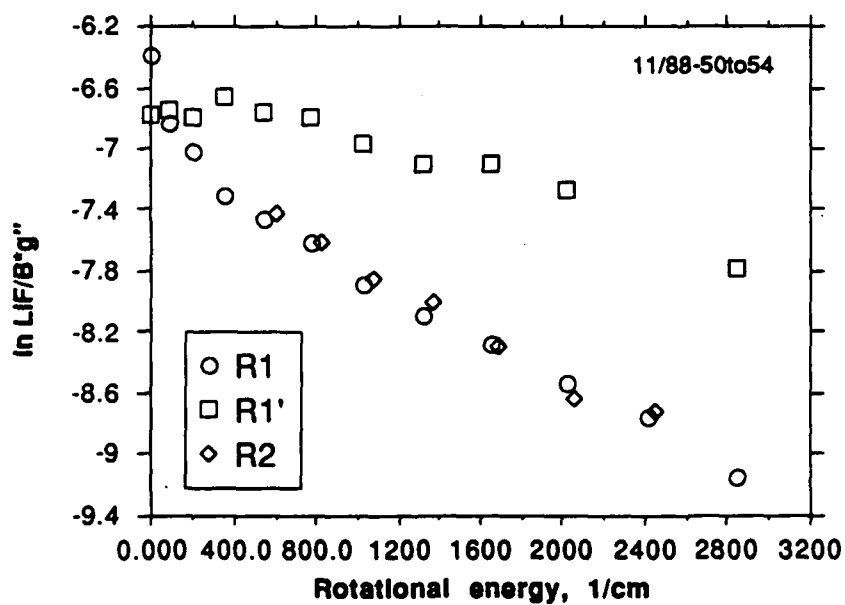


Figure 13. Same as Figure 12, but assuming non-saturation.

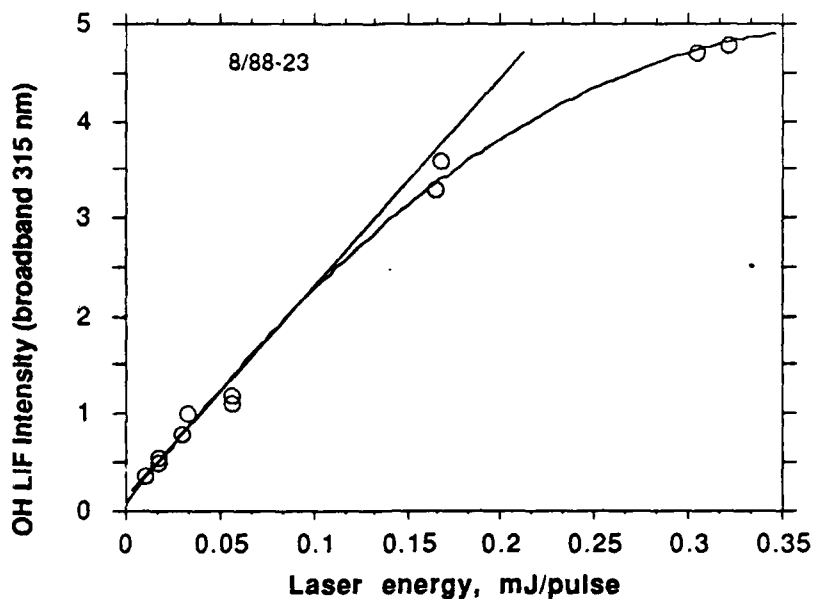


Figure 14. Saturation assessment. Broadband 315 nm detection, 281.915 nm excitation (OH 1,0 Q<sub>1</sub> 1 + R<sub>2</sub> 3). 50  $\mu$ m/3 mm slits, CH<sub>4</sub>/N<sub>2</sub>O flame, outer cone, 1 atm (air).

The effects of varying the excitation line on the structure of the LIF spectrum are shown in Figures 15-17. It can be seen that all the strongly excited lines are typically within the bandpass of Figure 6. To be outside the bandpass ( $>324$  nm), the observed 1,1 band lines would have to be P<sub>1</sub>, P<sub>2</sub> ( $N'' \geq 17$ ) or Q<sub>1</sub>, Q<sub>2</sub> ( $N'' \geq 24$ ). The structure of this LIF spectrum is, of course, radically different from the OH emission spectrum from the flame, an example of which is shown in Figure 18. For comparison purposes, the LIF spectra in the 0,0, 1,0, and 0,1 bands resulting from OH 0,0 excitation are shown in Figures 19-21. The narrowband filter has an important effect on the structure of the LIF reaching the detector. This is shown in Figures 22 and 23, where the emission spectrum from the flame is shown with and without the filter present. Note that the filter attenuates the R branches of the 0,0 band severely. The filter also affects the 1,1 band slightly, as can be seen by comparing Figures 15 and 24. The effect the filter has on LIF temperature measurements is not immediately obvious, so the filter was used during some of the excitation scans described in the next paragraph to determine the influence of the filter.

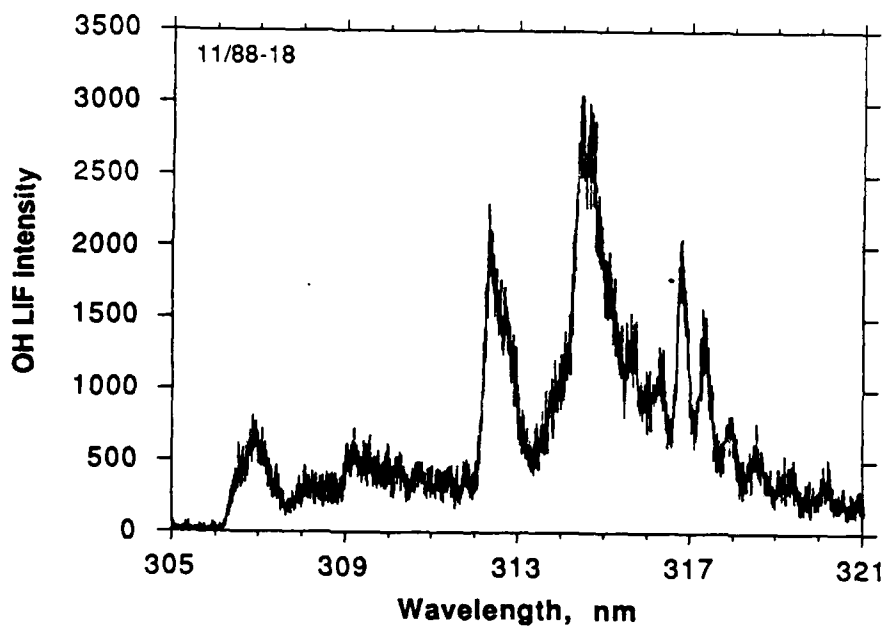


Figure 15. OH LIF spectrum, 1.0 R<sub>1.5</sub> excitation. Conditions similar to Figure 2 with 300-gr/mm grating.

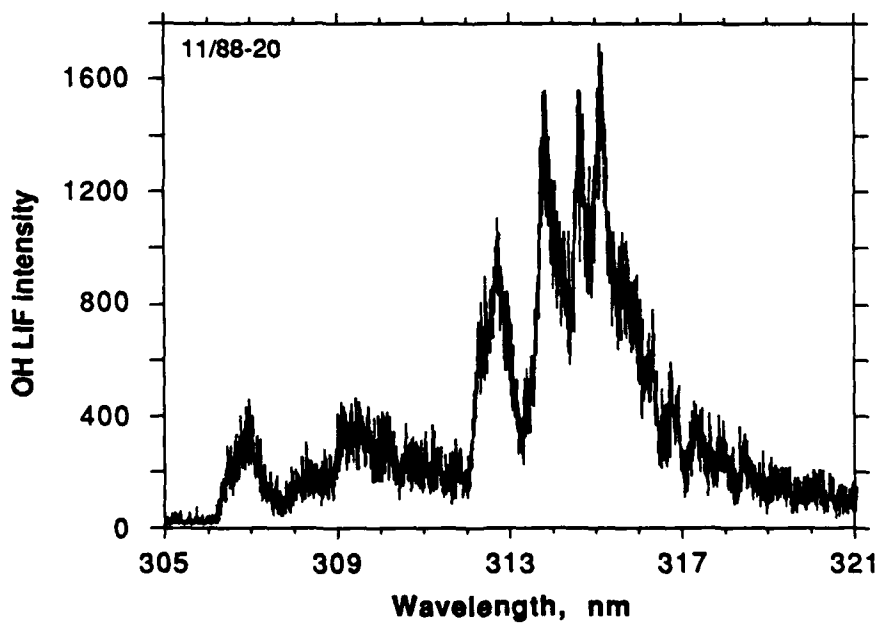


Figure 16. OH LIF spectrum, 1.0 R<sub>1.2</sub> excitation. Conditions same as Figure 15.

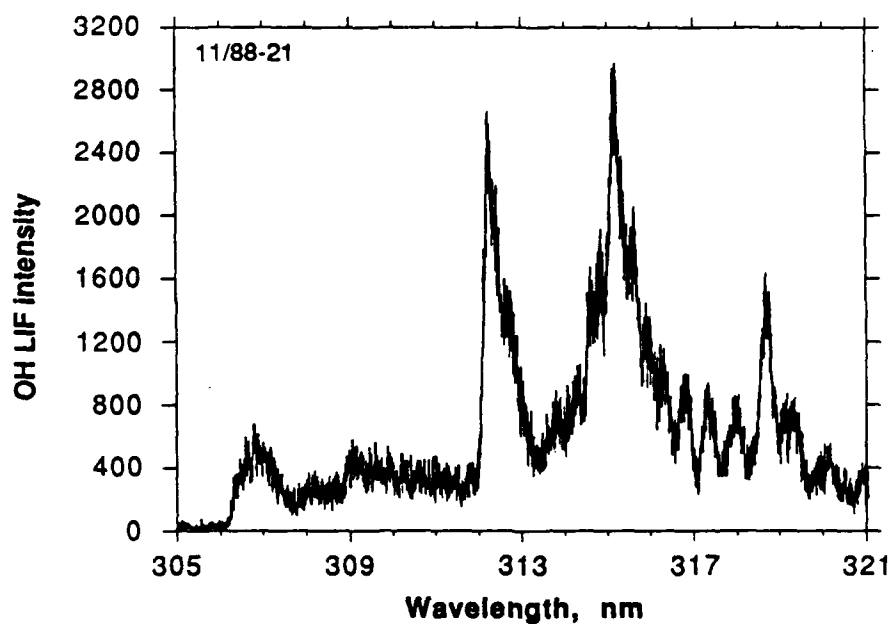


Figure 17. OH LIF spectrum. 1.0 R<sub>1</sub> 8 excitation. Conditions same as Figure 15.

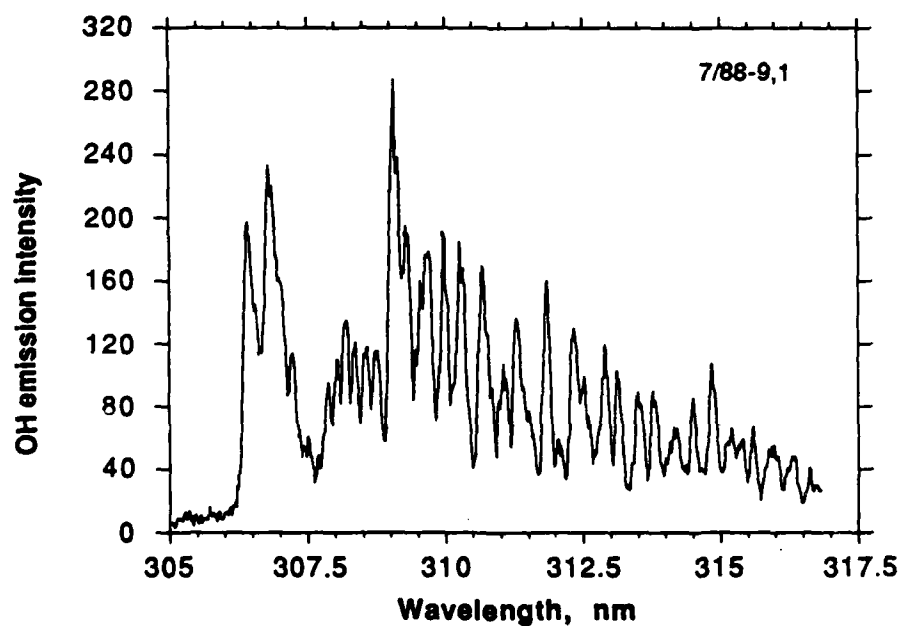


Figure 18. OH emission spectrum. CH<sub>4</sub>/N<sub>2</sub>O flame, Reticon detector, 700 pixels, 0.0175 nm/pixel dispersion, 500/200  $\mu$ m slits, 0.2 sec exp. time.



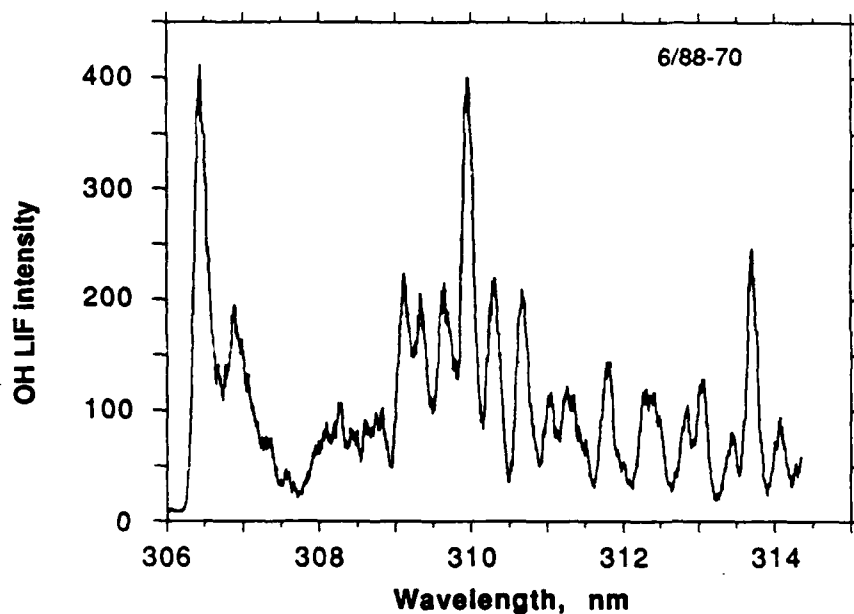


Figure 19. OH 0.0 LIF spectrum. 0.0 R<sub>1</sub> 8+R<sub>1</sub> 10 excitation (306.36 nm). CH<sub>4</sub>/N<sub>2</sub>O flame, 1 atm (air), outer cone, 0.03 mJ/pulse in flame, 50  $\mu$ m slits, 1200-gr/mm grating.

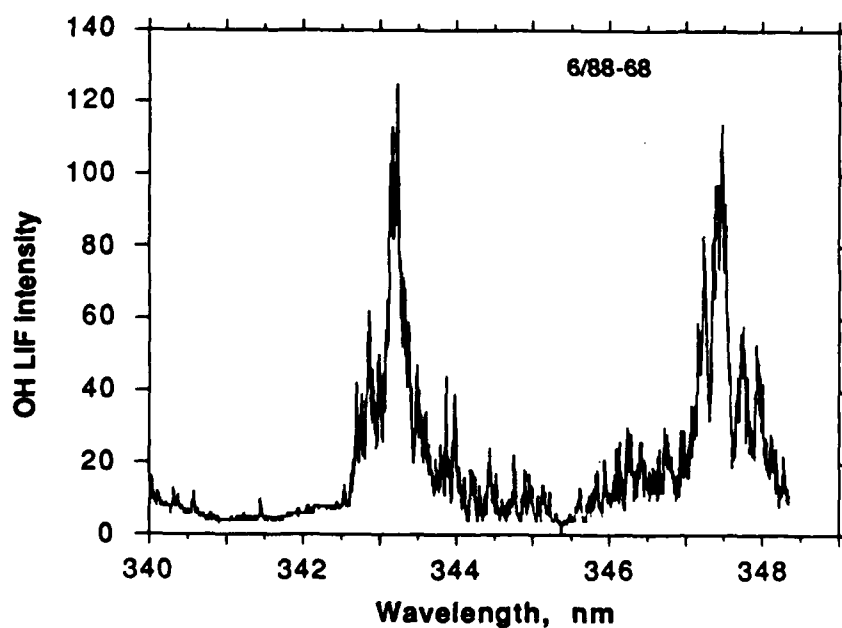


Figure 20. OH 0.1 LIF spectrum. Same conditions as Figure 19.

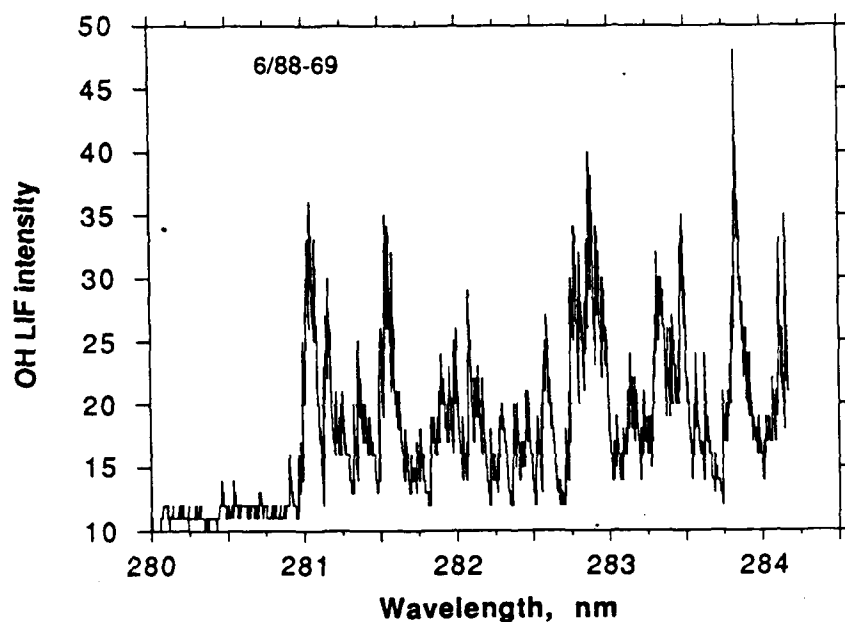


Figure 21. OH 1.0 LIF spectrum. Same conditions as Figure 19.

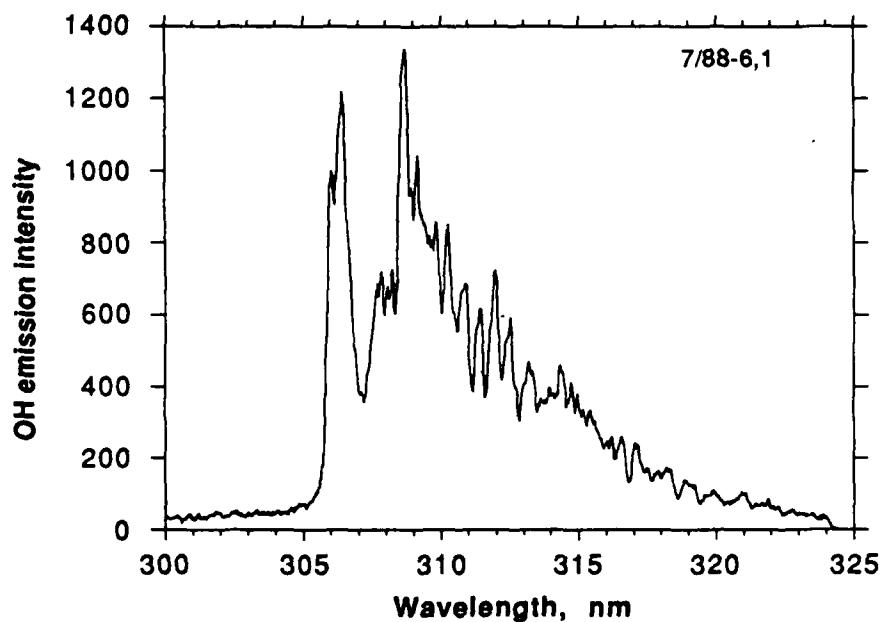


Figure 22. OH emission spectrum. Same conditions as Figure 18 except 1200-gr/mm grating (0.035 nm/pixel dispersion).

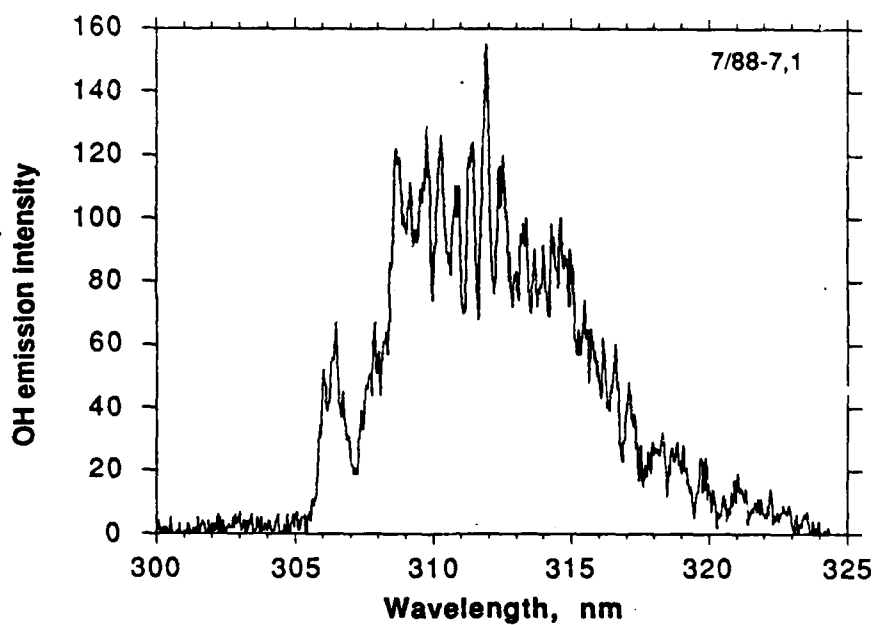


Figure 23. OH emission spectrum through interference filter. Same conditions as Fig. 22.

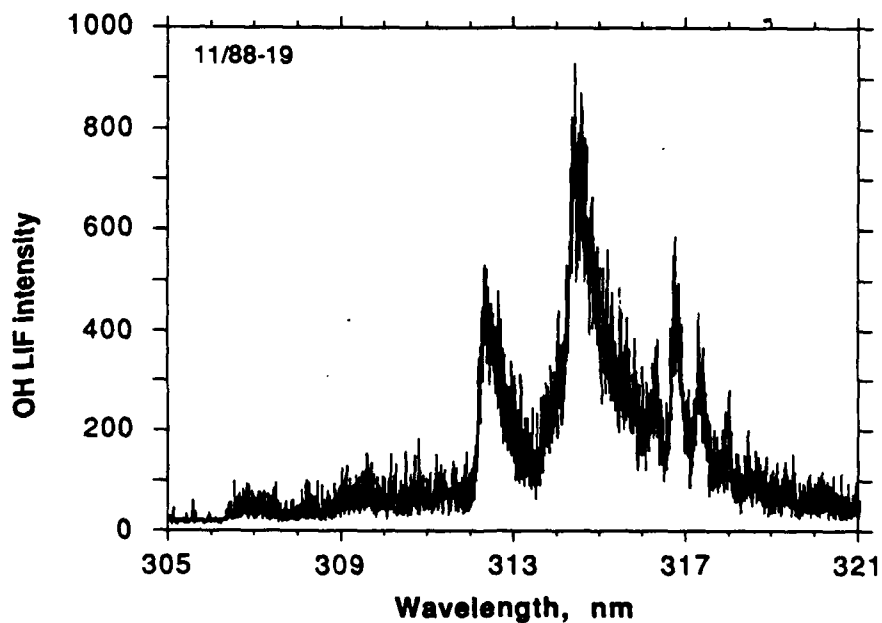


Figure 24. OH LIF spectrum (1.0 R<sub>1.5</sub> excitation) through interference filter. Conditions same as Figure 15.

To examine the effect of various detection parameters on OH LIF temperature measurements, excitation scans of the length of that in Figure 7 were too time-consuming. For this reason a shorter scan over the OH 1,0  $R_1$  and  $R_1'$  branches from approximately 281.1 to 281.35 nm was employed. An example of such an excitation scan and the resulting Boltzmann plot for the  $R_1$  branch ( $R_1 2 - R_1 8$ ) is shown in Figures 25 and 26. Unfortunately, this truncated scan gave temperatures that were consistently lower than those of the more complete scan of Figure 7. For example, using only the  $R_1 2$  to  $R_1 8$  lines of Figures 7 and 10 gave a best-fit temperature of 1579 K, while using  $R_1 3$  to  $R_1 8$  gave a best-fit temperature of 1749 K (unsaturated assumption). It appears best to avoid low  $J''$  lines in this type of measurement altogether. A more complete analysis than the one below would use a larger range of lines to obtain more accurate data. For the purposes of this study, a limited scan was deemed to be appropriate. For better accuracy, the data should be corrected for partial saturation also. For the limited purposes of this study, the data were not corrected. Instead, the OH LIF excitation scans were reduced for both the saturated and unsaturated limiting cases, and the effects of detection gate width and timing were assessed by the changes in the limiting case behavior.

The temporal location of the detection gate (relative to the laser pulse) should have an important influence on the characteristics of the OH LIF excitation scans and thus could have an important influence on the OH LIF temperature measurements. In the results discussed thus far, a 30-ns detection gate was used, with the timing adjusted so that the LIF intensity was a maximum. This occurred at a gate delay (relative to a trigger pulse from the laser power supply) of 1.20  $\mu$ s. For a 10-ns gate width, the maximum OH LIF intensity occurred at essentially the same delay setting. For a 10-ns gate width, changing this delay setting by  $\pm 0.01$   $\mu$ s (10 ns) reduced the LIF intensity by 50%. The effect of this change on OH LIF excitation scans is shown in Figures 27 and 28. With the earlier detection gate (Figure 27), the excitation scan approached the unsaturated limiting case more closely than the baseline excitation scan (Figure 26), as shown by the closeness of the unsaturated  $R_1$  and  $R_1'$  branches on the Boltzmann plot. With the later detection gate (Figure 28), the Boltzmann plots show more saturation. The trend is steady; as shown in Figure 29, a summary of Figures 26-28. With the short scans employed ( $N''=3-8$ ), eliminating one of the points on the Boltzmann plots often changed the best fit temperature by hundreds of degrees. Thus, the accuracy of these scans is too low to draw definitive conclusions from this data. Within the accuracy of this method, the excitation scans for the 10 and 30-ns baseline gate widths gave identical temperatures. Changing the center of the detection bandpass to 312.5 and 317.5 nm (from 315 nm) also had a negligible effect on the rotational temperature found from the excitation scans. In early experiments with a 3-nm detection bandpass, a strong effect of the location of the detection bandpass (314-316 nm) was found. With the 20-nm bandpass used for most of the OH LIF temperature measurements, this effect was not seen. In most cases, the addition of the 313-nm filter also had a negligible effect on the excitation scan temperature. A notable exception was the 10-ns "early" gate, where the addition of the filter had a large effect on the temperatures, as can be seen by comparing Figures 27 and 30. The baseline 10 and 30-ns cases showed little effect of adding the filter. Thus, under certain conditions, a narrowband filter (or a narrower detection bandpass), may be used if care is taken to assure that the narrower bandpass is not affecting the temperature measurement. The main conclusion to be drawn from this work on the calibration flame is that careful attention must be paid to the saturation characteristics of the system to obtain reliable temperature measurements.

This type of excitation scan requires several minutes as a minimum to obtain accurate data. In transient experiments where the necessary time for an excitation scan is not available, typically two experiments are performed with two excitation lines (denoted by subscript 1 and 2); such that  $kT/hc = (E_{r1} - E_{r2}) / [(I_{fl}/g''B)_1 / (I_{fl}/g''B)_2]$  in the unsaturated case and  $kT/hc = (E_{r1} - E_{r2}) / \{ [I_{fl}(1/g'' + 1/g')]_1 / [I_{fl}(1/g'' + 1/g')]_2 \}$  for the saturated case. In a good example of the two-line technique, Parr & Parr at NWC obtained two-dimensional images of OH LIF  $T_r$  in a laser-driven atmospheric pressure propellant flame by exciting two lines in separate experiments and dividing the resulting digital images (Ref. 13). Of course, any differences between the two experiments would lead to errors in the temperature profile.

The two-line procedure involves several assumptions, aside from questions of saturation. Although broadband collection assures collection of the LIF from an entire band when done properly (Ref. 28), if the various upper rotational levels have different quenching behavior dependent on rotational level, the measurements would be biased and give incorrect temperatures. There is some evidence that quenching does vary with rotational level in some molecules, including OH (Ref. 32,42). To correct for this problem, Cattolica (Ref. 34) uses the two-line excitation method, but excites the same upper state from two different lower levels (e.g.,  $Q_{21} 9$  and  $S_{21} 7$ ); thus the quenching behavior would be the same for the two lines. This approach avoids the quenching problem. However, it can have temperature sensitivity problems since the two levels are of relatively close rotational energy; the maximum sensitivity is obtained by means of relatively weak satellite transitions (Ref. 34). This same scheme is employed when making temperature measurements using seeded species such as Tl (Ref. 9,10). Most of the verification of the excitation scan technique has been done at low pressures, so there is some question as to the application of this technique to high pressure flame diagnostics. The effects of pressure on this technique merits further study.

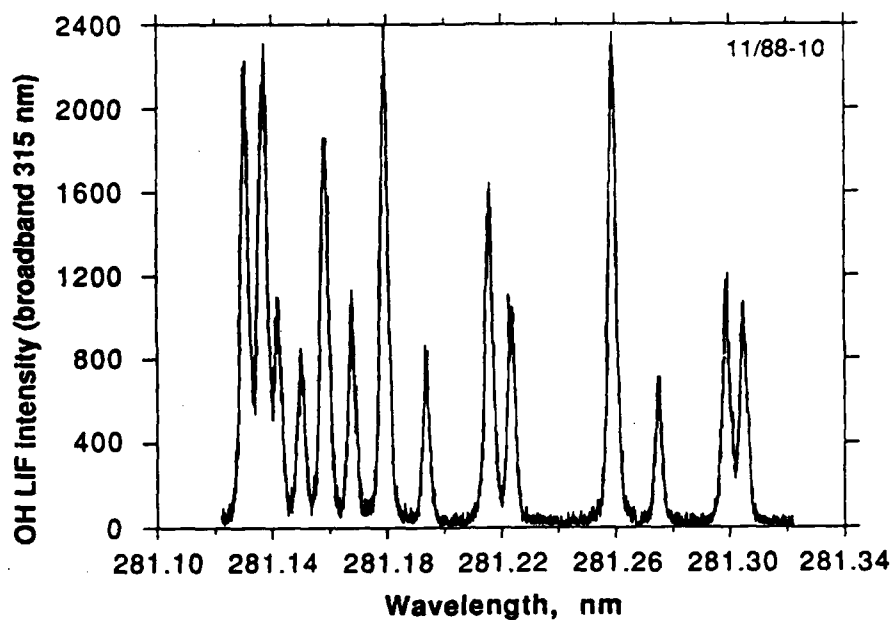


Figure 25. OH LIF excitation scan with broadband collection centered at 315 nm. Same conditions as Figure 7 except 0.002 mJ/pulse laser energy in flame and 10 ns gate width.

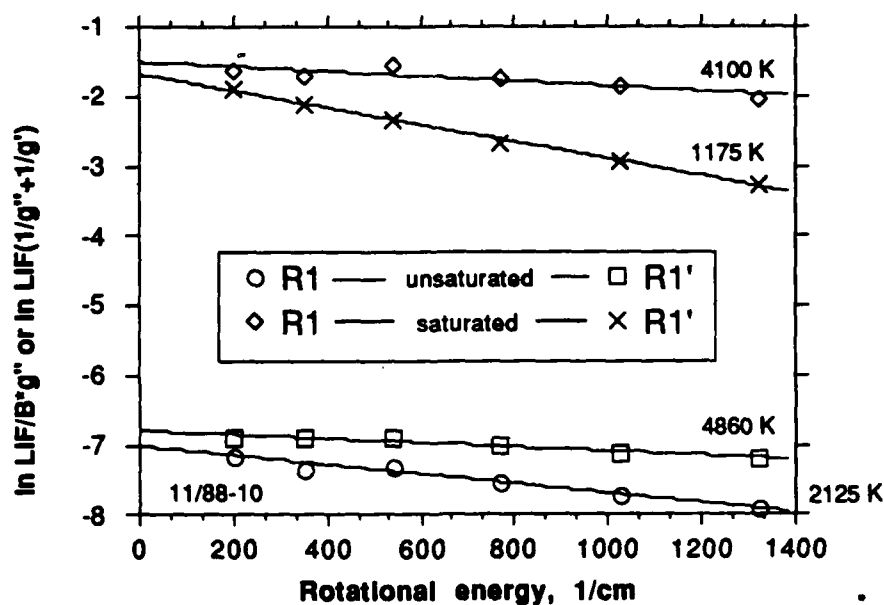


Figure 26. Boltzmann plot of data from Figure 25.

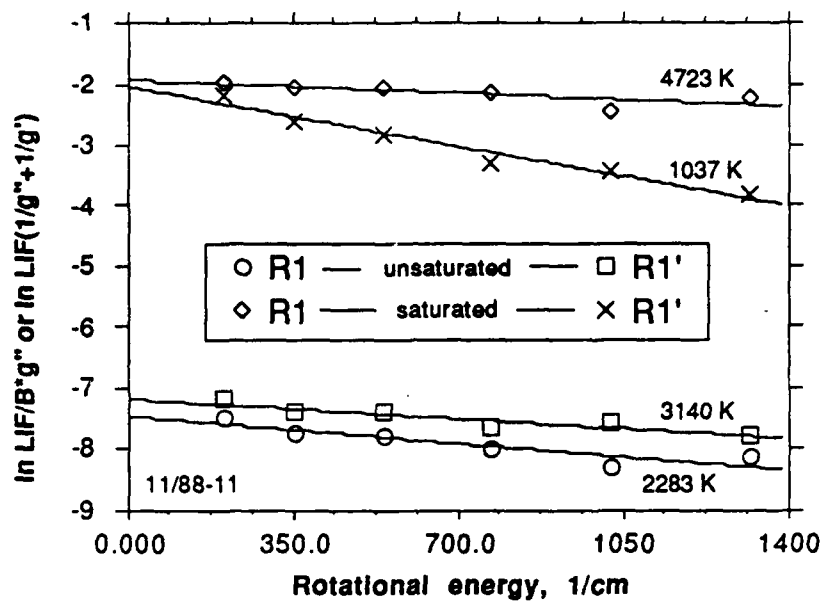


Figure 27. Effect of detection gate delay on OH LIF excitation scan temperature. Same conditions as Figure 26 except gate delay reduced by  $\sim 0.01 \mu s$ .

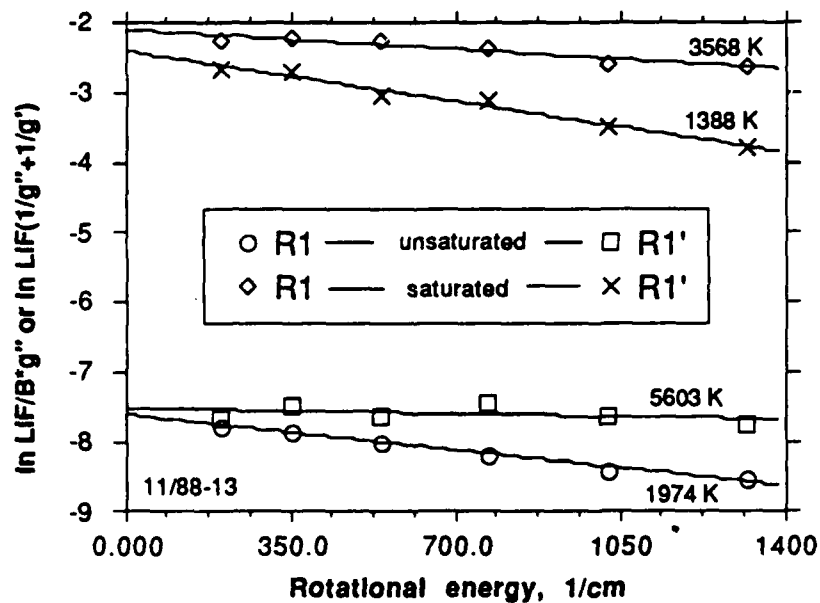


Figure 28. Effect of detection gate delay on OH LIF excitation scan temperature. Same conditions as Figure 26 except gate delay increased by  $\sim 0.01 \mu s$ .

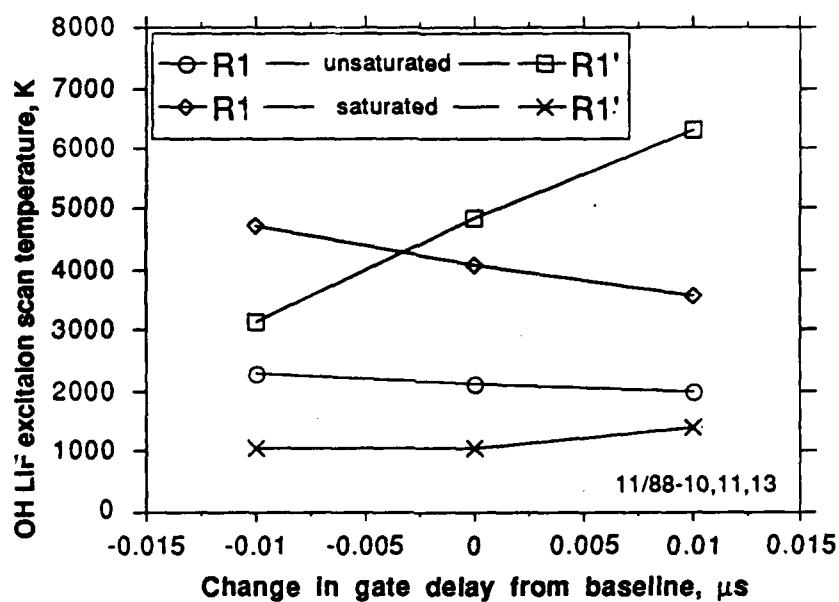


Figure 29. Effect of gate delay on OH LIF excitation scan temperature. Data from Figures 26-28.

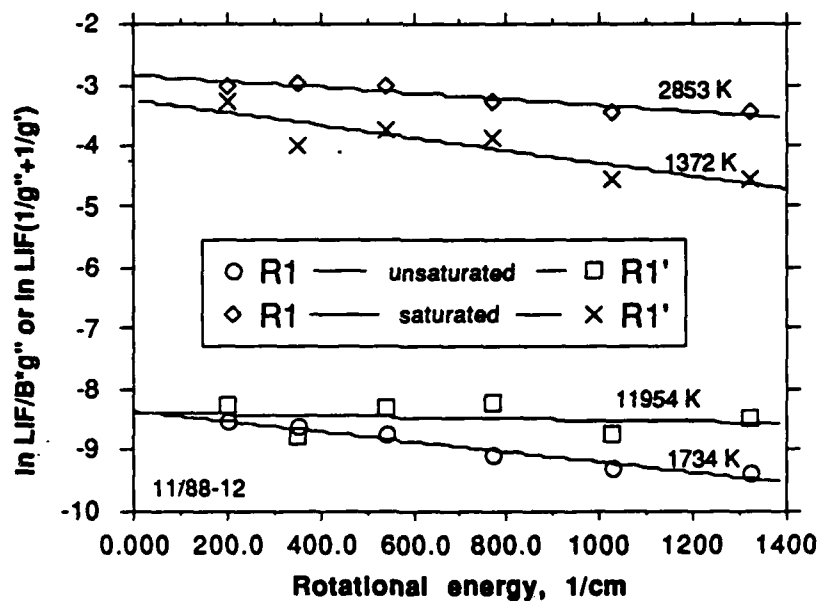


Figure 30. Effect of 313-nm filter on OH LIF excitation scan temperature. Conditions same as Figure 27 except filter added to collection optics.



## PROPELLANT FLAME EXPERIMENTS

For the propellant flame measurements described in this paper, it was decided that the greater temperature sensitivity obtainable by exciting strong transitions with differing upper levels compensated for the errors involved in neglecting quenching differences. The two lines selected for the propellant experiments were  $R_1 4$  and  $R_1 10$ . The temperature response of these two lines is illustrated in Figure 31. The propellant experiments were performed by allowing the propellant to burn down through the laser beam, as idealized in Figure 32. This is the same as keeping the propellant surface at a constant height and moving the laser beam and collection optics up through the flame (but much simpler). To perform the temperature measurement, average OH LIF profiles from  $R_1 4$  and  $R_1 10$  excitation were obtained from multiple experiments; the resulting profiles were then ratioed and converted to a temperature profile point-by-point using Fig. 31. Several things should be noted in Figure 32. For a given propellant burn rate, the number of data points in a given flame region is determined by the laser repetition rate. For example, for a propellant burn rate of 2 mm/s, a 40 Hz laser repetition rate implies that the propellant surface has regressed 50  $\mu\text{m}$  between data points. Thus a premium is placed on high laser repetition rates in such a "burn-through" experiment. This type of experiment is procedurally identical to a propellant micro-thermocouple measurement, except that no data is collected in the condensed phase. Also, there is a region near the propellant surface where there is only partial transmission of the laser beam. From a consideration of the geometry of the experiment, this region should be 100-200  $\mu\text{m}$  in thickness for a perfectly flat propellant surface. A surface that is level but "rough", such as the surface of an AP composite propellant, would increase this interaction zone thickness. A non-level surface would compromise the data further. As a result, LIF measurements inside this zone are rather suspect. LIF measurements in this region could perhaps be normalized by the transmission, although in optically thick flames this procedure does not work well.

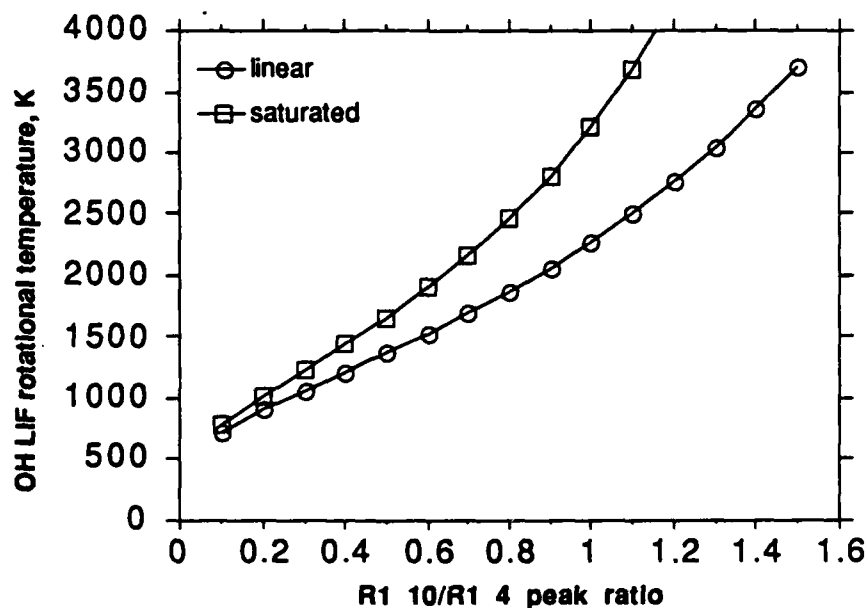


Figure 31. Temperature sensitivity of OH 1.0  $R_1 4$  and  $R_1 10$  excitation.

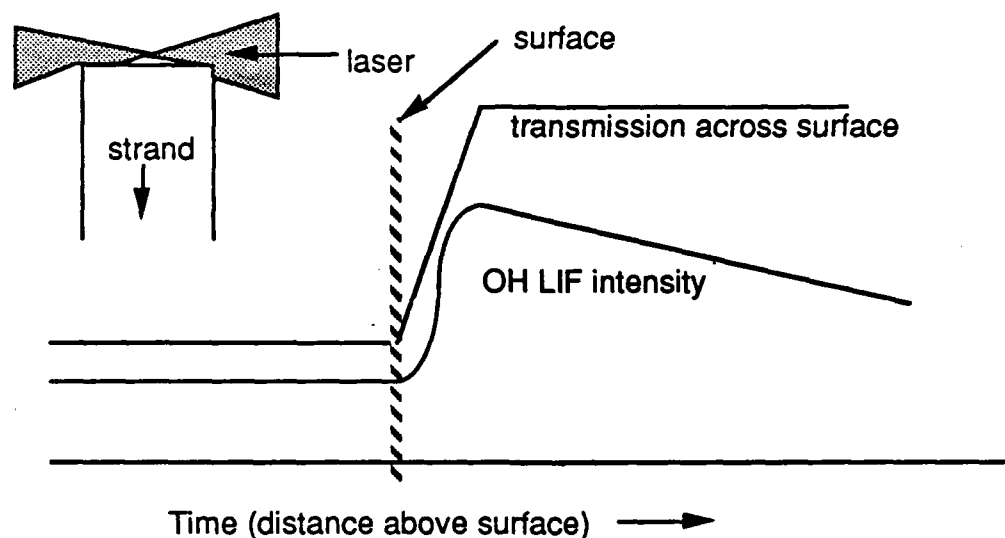


Figure 32. Schematic of OH LIF "burndown" experiments.

Once the LIF profiles from  $R_1 4$  and  $R_1 10$  excitation are collected, a distance scale (above the propellant surface) is assigned; this procedure is prone to some error because the precise location of the surface is occasionally not obvious. The profiles can then be normalized as described in the previous section and divided, producing a temperature profile. For example, the "OH LIF" profile in the flame above an 87% AP1 propellant ( $R_1 4$  excitation) is shown in Figure 33 for two experiments. Such profiles were obtained also in HMX1 propellant flame at 1.5 MPa (200 psig) and in the AN1 propellant flame at 0.8 MPa (100 psig), as illustrated in Figures 35 and 36. The laser attenuation in the AN1 flames was so large that temperature measurements in this propellant flame were abandoned. The attenuation can be seen by comparing the transmission scales of Figures 11 and 12, taken with the same laser power. Even in the relatively "clean" AP and HMX flames, the laser attenuation was often  $>50\%$  at pressures above 1-2 MPa (150-300 psig) (Ref. 12,17,18). The attenuation in the HMX2 propellant flame was also very large. 5-10 profiles were collected from both  $R_1 4$  and  $R_1 10$  excitation in the AP1 and HMX1 propellant flames over a period of several days. The laser wavelength was periodically checked with the calibration flame to ensure that the laser was tuned to the correct line. The results were relatively inconsistent, with large variations (factor of  $>2$ ) in the peak "OH LIF" intensity, although most of the profiles were superficially similar. The variations from experiment to experiment can be seen in Figure 33. When the laser was detuned from resonance (no OH LIF seen in the calibration  $\text{CH}_4/\text{N}_2\text{O}$  flame), and an identical "burn-through" experiments were performed, the results shown in Figures 37 and 38 were obtained. Obviously, there is a problem. The wide detection bandpass which the temperature measurement requires was allowing large amounts of spurious laser scattering from the flame to contaminate (actually, overwhelm is probably more accurate) the OH LIF signal, leading to poor results. This result is not surprising when one considers that spurious scattering was a problem in CN LIF experiments where the collection bandwidth (421.5 nm excitation, 388.3 nm detection) was  $\sim 0.05$  nm (Ref. 12,18). Maintaining a wide detection

bandpass while maintaining a high level of light rejection is the major stumbling block to the application of this technique to high pressure solid propellant flames. One possibility would be to use a double or triple spectrometer to increase the light rejection. Another possibility might be to use a narrower bandpass, carefully calibrated (in the previously mentioned high pressure flame) to allow correction of the narrowband results to yield accurate temperatures.

Additional propellant experiments were performed with the previously described interference filter (313 nm, 11-nm bandpass), in the collection path to aid in light rejection. As can be seen by comparing Figure 38 ( $R_1$  10 excitation) and 39 ( $R_1$  5 excitation) with Figure 40 (laser detuned from resonance), the addition of the filter has enhanced the light rejection enough that OH LIF is apparent above 1 mm in the AP propellant. Between the surface and 1 mm, spurious (non-OH LIF) scattering is still dominant. Although the results are unreliable, rough temperature estimates can be made from 2-4 mm above the surface from Figures 38 and 39, yielding 1700-1800 K. Considering the biases discussed in the previous section, the "corrected" (actual) temperature could be  $\sim 500$  K higher. At a distance from the surface of 2-4 mm, it seems reasonable to expect that the flame temperature should be near the adiabatic flame temperature of the propellant ( $\sim 2900$  K). Although the data is suspect, it suggests that the flame temperature in the AP1 propellant flame is well below the adiabatic flame temperature. This discussion has assumed that the AP1 propellant flame is homogeneous on the scale of the collection volume, which can be approximated as a slab of 100  $\mu\text{m}$  in thickness and depth and 2 mm in length. On this scale, the heterogeneous nature of the propellant may persist into the flame. This data can be compared to the temperatures inferred from OH emission spectra in this same propellant flame by Campbell (Ref. 11). He found that the rotational temperature of the excited electronic ( $A^2\Sigma$ ) state of OH in the AP1 propellant flame at 0.8 MPa at  $\sim 2$  mm above the surface was  $2900 \pm \sim 200$  K, very close to the adiabatic flame temperature. As pressure increased, the emission temperatures also increased. His calculations were based on comparisons of computer-generated emission spectra and actual emission spectra in the propellant flame. The experimental spectra were collected with the Reticon diode array detector as in Fig. 18. The emission temperatures were much more reproducible than the LIF temperatures, although the interpretation of the emission temperatures was made more difficult by possible self-absorption effects and non-equilibrium rotational distributions (Ref. 11). Also, the temperature of the OH  $A^2\Sigma$  state may not be the same as that of the much more populous ground ( $X^2\Pi$ ) state. LIF experiments measure the temperature of the  $X^2\Pi$  state (Ref. 8). It remains to be proven whether or not the OH  $A^2\Sigma$  temperature is the same as the translational temperature in the flame, as is often assumed (Ref. 53,54).

A similar series of experiments was performed in the HMX1 propellant flame at 1.5 MPa (200 psig), as shown in Figures 41-43. In this propellant flame, the OH LIF signal is indistinguishable from the scattering. The reproducibility of the data is also poor, as can be seen in Figures 41-43. The lack of OH LIF signal is not surprising, since the equilibrium OH concentration in the HMX1 flame at the adiabatic flame temperature is about 20 times smaller than that in the AP1 propellant flame. Thus, the HMX1 flame is a more difficult subject for OH LIF measurements. Successful temperature measurements have been recently reported in a HMX1 propellant flame using CARS (Ref. 14). The temperature several millimeters from the surface was found to be near the adiabatic flame temperature (2600 K).

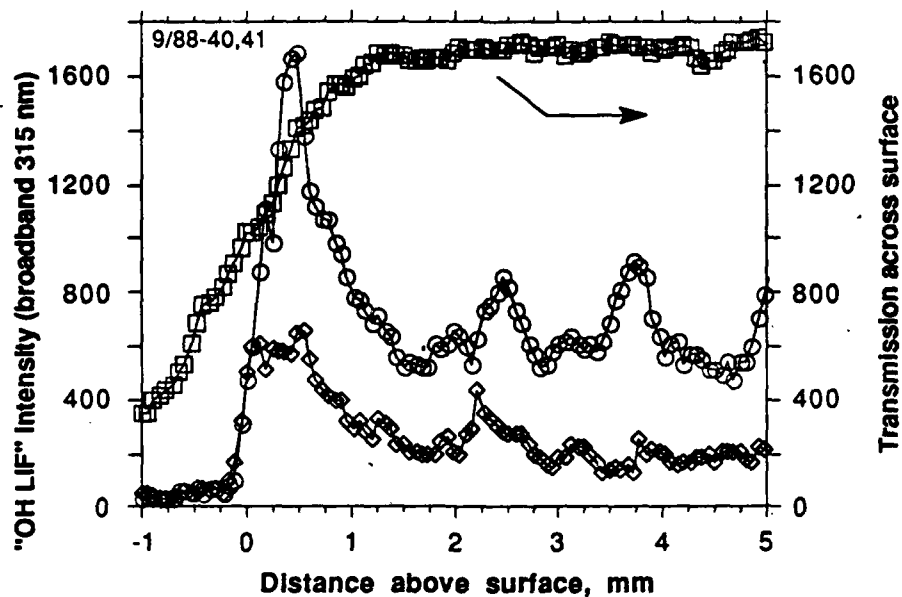


Figure 33. "OH LIF" profile in propellant flame. AP1 propellant, 0.5 MPa (50 psig), 0.015 mJ/pulse in flame, 40 Hz,  $R_1$  10 excitation (281.537 nm), 50  $\mu$ m/3 mm slits.

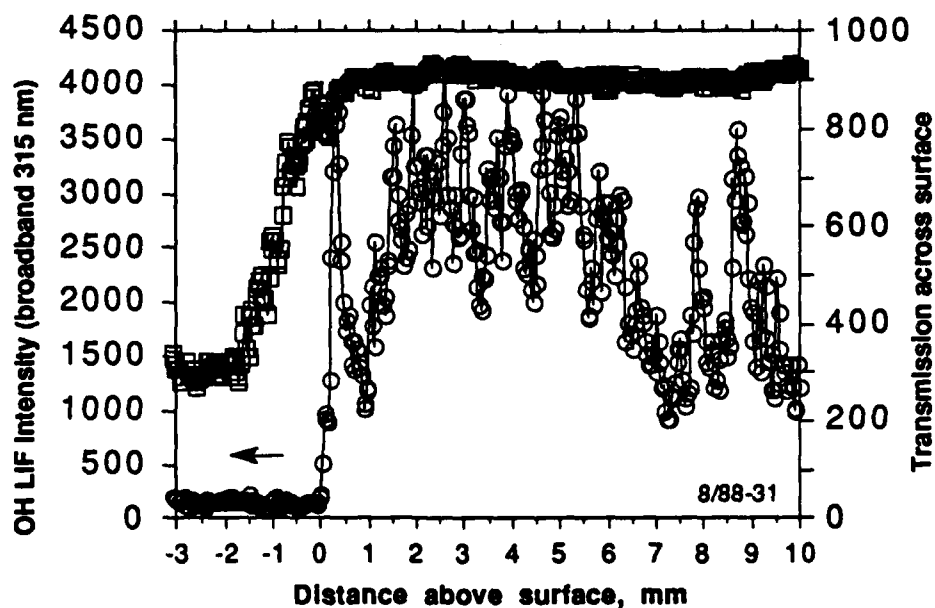


Figure 34. "OH LIF" profile in propellant flame. HMX1 propellant, 1.5 MPa (200 psig), 0.15 mJ/pulse in flame, 40 Hz,  $R_1$  10 excitation (281.537 nm), 50  $\mu$ m/3 mm slits.

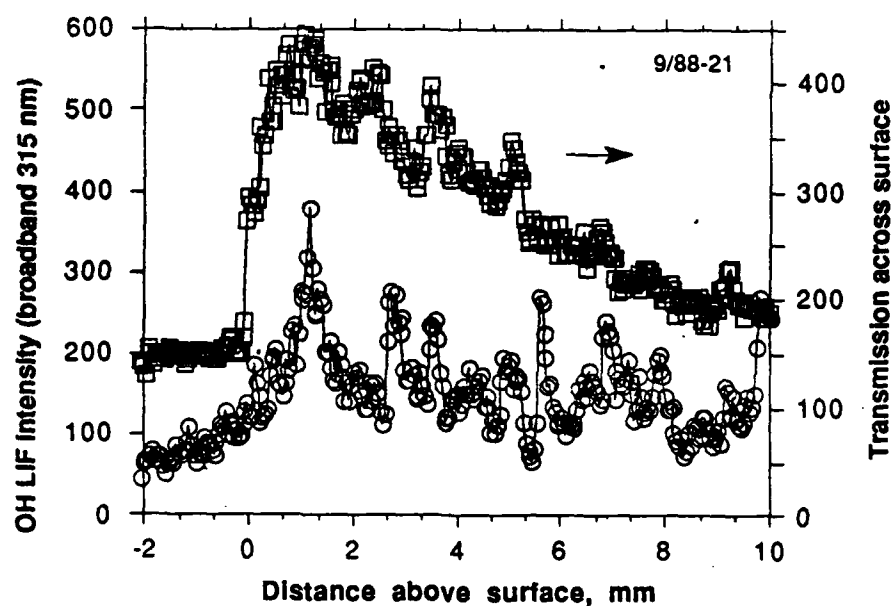


Figure 35. "OH LIF" profile in propellant flame. AN1 propellant, 0.8 MPa (100 psig), 0.15 mJ/pulse in flame (unattenuated), 40 Hz,  $R_1$  10 excitation (281.537 nm), 50  $\mu$ m/3 mm slits.

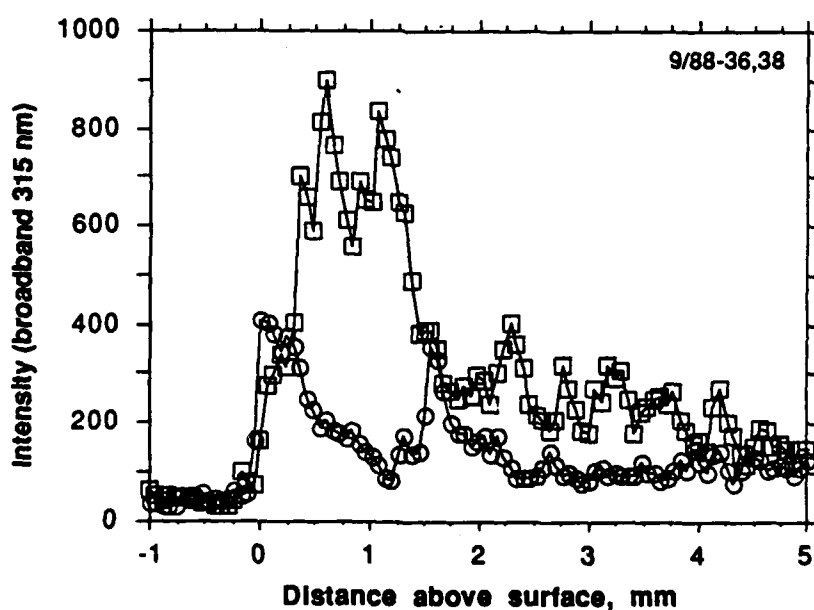


Figure 36. "OH LIF" profiles in propellant flame. AP1 propellant, 0.5 MPa (50 psig), 0.015 mJ/pulse in flame, 40 Hz, laser detuned from OH line (281.48 nm), 50  $\mu$ m/3 mm slits.

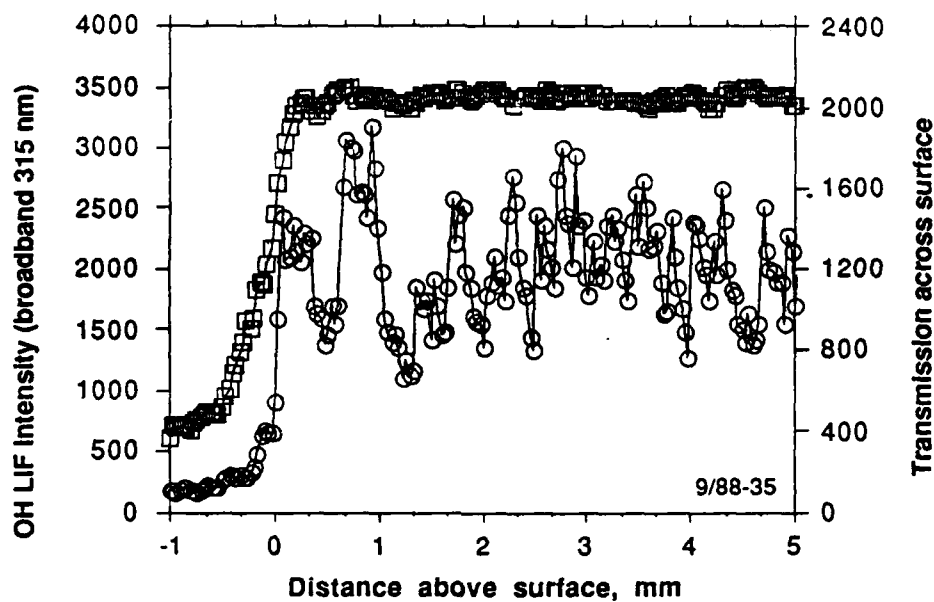


Figure 37. "OH LIF" profile in propellant flame. HMX1 propellant, 1.5 MPa (200 psig), 0.12 mJ/pulse in flame, 40 Hz, laser detuned from OH line (281.48 nm), 50  $\mu$ m/3 mm slits.

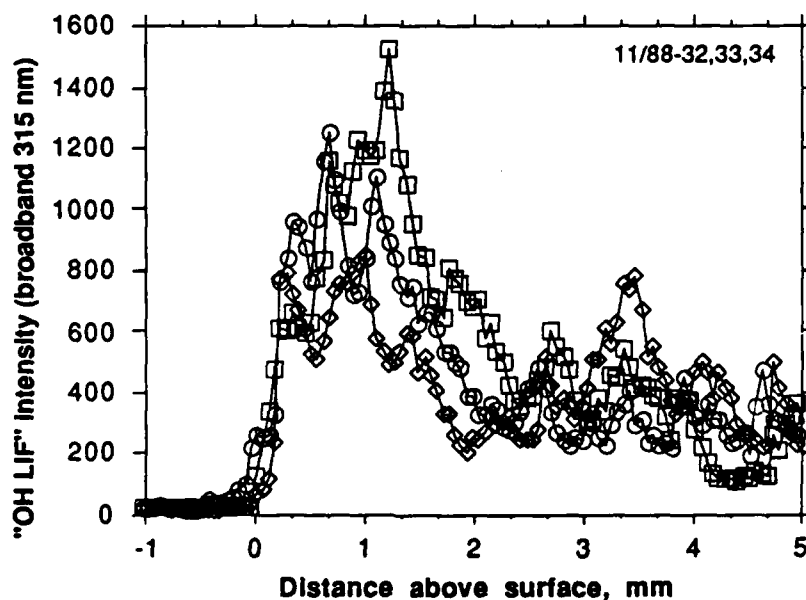


Figure 38. "OH LIF" profiles in propellant flame with 313 nm filter. AP1 propellant, 0.5 MPa (50 psig), 0.08 mJ/pulse in flame, 40 Hz, 3 pulse average,  $R_1$  10 excitation, 30  $\mu$ m/3 mm slits.

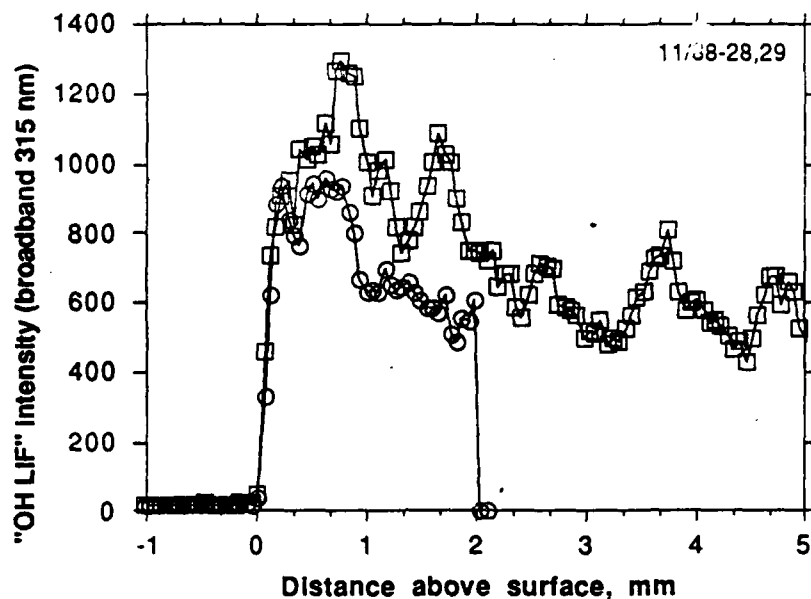


Figure 39. "OH LIF" profiles in propellant flame with 313 nm filter. AP1 propellant, 0.5 MPa (50 psig), 0.08 mJ/pulse in flame, 40 Hz, 3 pulse average,  $R_1$  5 excitation, 30  $\mu$ m/3 mm slits. One experiment was truncated by experimental difficulties when the laser was ~2mm above the surface.

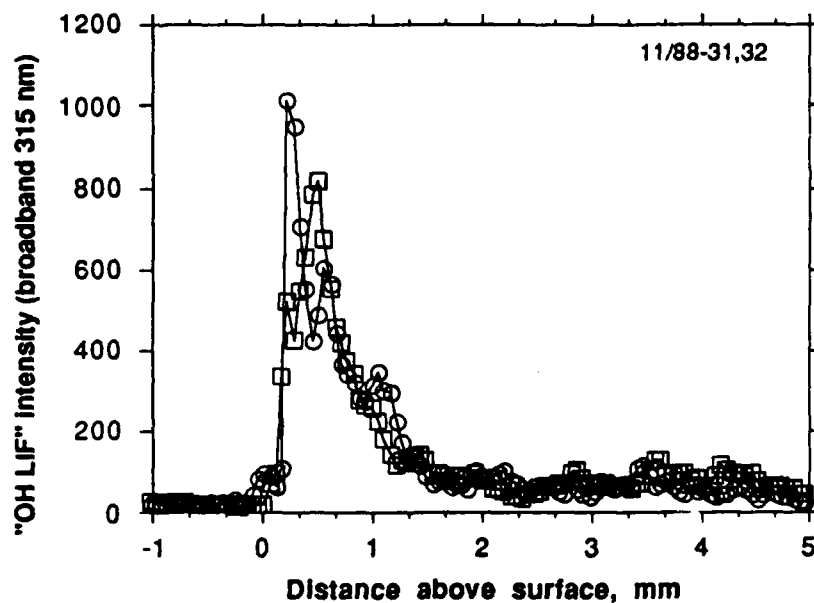


Figure 40. "OH LIF" profiles in propellant flame with 313 nm filter. AP1 propellant, 0.5 MPa (50 psig), 0.08 mJ/pulse in flame, 40 Hz, 3 pulse average, laser detuned from OH lines, 30  $\mu$ m/3 mm slits.

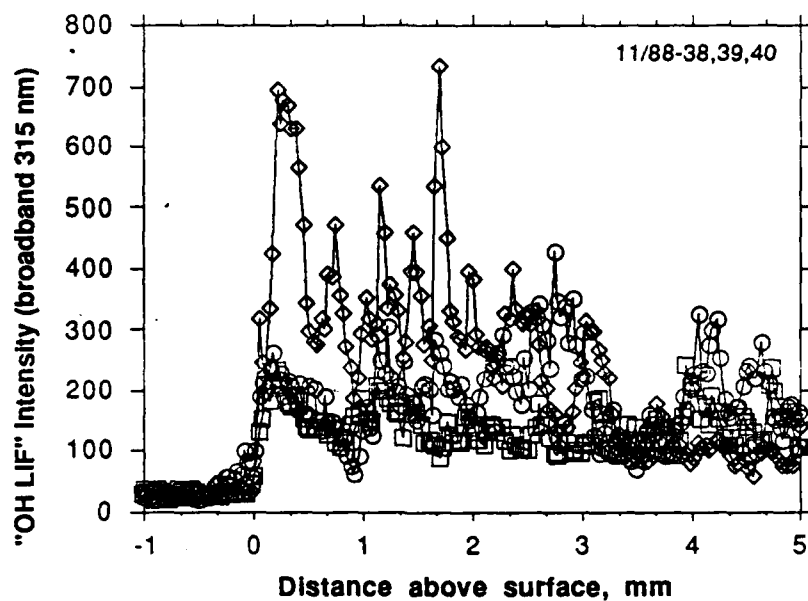


Figure 41. "OH LIF" profiles in propellant flame with 313 nm filter. HMX1 propellant, 1.5 MPa (200 psig), 0.08 mJ/pulse in flame, 40 Hz, 3 pulse average,  $R_1$  5 excitation, 30  $\mu$ m/3 mm slits.

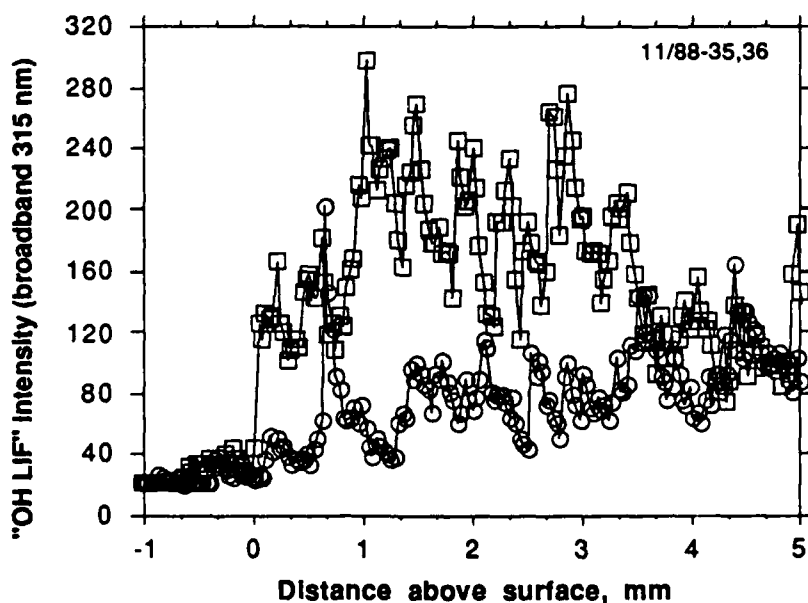


Figure 42. "OH LIF" profiles in propellant flame with 313 nm filter. HMX1 propellant, 1.5 MPa (200 psig), 0.08 mJ/pulse in flame, 40 Hz, 3 pulse average,  $R_1$  10 excitation, 30  $\mu$ m/3 mm slits.



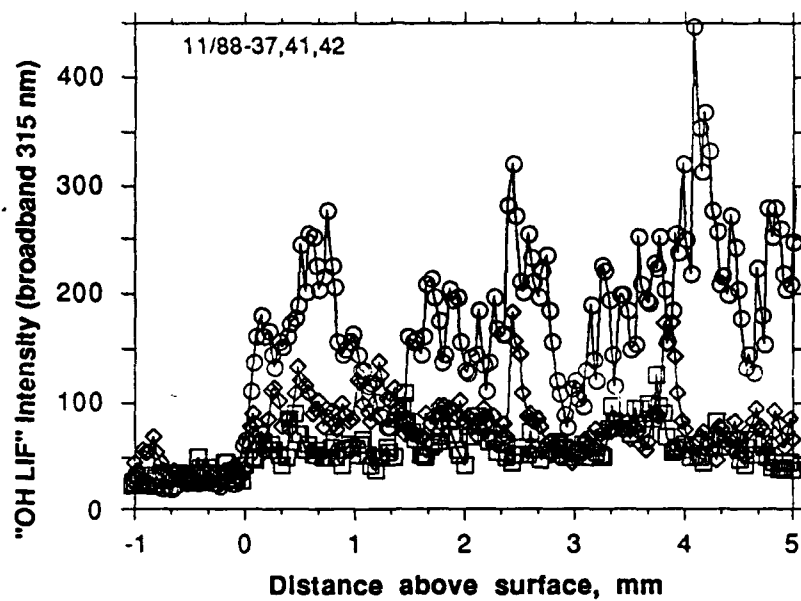


Figure 43. "OH LIF" profiles in propellant flame with 313 nm filter. HMX1 propellant, 1.5 MPa (200 psig), 0.08 mJ/pulse in flame, 40 Hz, 3 pulse average, laser detuned from OH lines, 30  $\mu$ m/3 mm slits.

## CONCLUSIONS AND RECOMMENDATIONS

This report has described an attempt to use OH LIF to measure temperature in high pressure solid propellant flames. The techniques used were similar to those successfully employed by Parr and Parr (Ref. 13) to measure temperature in atmospheric pressure laser-driven propellant "flames." When applied to higher pressure propellant flames, however, the requirements of a large (20 nm) detection bandpass to obtain accurate measurements (Ref. 28, 50) created severe problems with light rejection. The attenuation of the diagnostic laser beam caused by the optical thickness of the propellant flames created very large signals at the laser wavelength (281 nm), which were difficult to separate from the desired LIF signal ( $315 \pm 10$  nm). Using the combination of an interference filter and a spectrometer (300 gr/mm grating with a 3-mm rear slit), wide bandpass detection with relatively high light rejection could be accomplished, although only marginally successful results could be obtained in an AP-based propellant with its high OH concentration. OH LIF temperature measurements in HMX-based propellant flames were unsuccessful. Because of the difficulty of the OH LIF temperature measurements in high pressure propellant flames, other temperature measurement techniques, such as CARS, may be more successful and should be pursued. Another option is NO LIF temperature measurements. NO has a much different vibro-rotational structure from OH, so it may be possible to accomplish the necessary wide bandpass detection (which would be much less than the 20 nm required for OH) with the necessary light rejection.

## REFERENCES

1. Cohen, N. S., "Review of Solid Propellant Burn Rate Modeling," AIAA Journal, Vol. 18, pp. 277-293, 1980.
2. Bizot, A., and Beckstead, M. W., "A Model for Double Base Propellant Combustion," paper presented at the 22nd Symposium (Int'l) on Combustion, Seattle, WA, August 1988.
3. Kubota, N., "Physicochemical Processes of HMX Propellant Combustion," 19th Symposium (Int'l) on Combustion, Combustion Institute, Pittsburgh, 1983, pp. 777-785.
4. Hatch, R. L., "Chemical Kinetics Modeling of HMX Combustion," 24th JANNAF Combustion Meeting, CPIA Publication 476, Volume I, pp. 383-391, 1987; Melius, C., "Theoretical Studies of the Chemical Reactions Involved in the Ignition of Nitramines," 24th JANNAF Combustion Meeting, CPIA Publication 476, Volume I, pp. 359-366, 1987.
5. Lengelle, G., Bizot, A., Duterque, J., and Trubert, J. F., "Steady-State Burning of Homogeneous Propellants," Chapter 7 (pp. 361-408) in Fundamentals of Solid Propellant Combustion, (Kuo, K., and Summerfield, M.(eds)), AIAA Progress in Astronautics and Aeronautics Series, Volume 90, AIAA, New York, 1984.
6. Fetherolf, B. L., Kim, J. U., Litzinger, T. A., and Kuo, K. K., "CO<sub>2</sub> Laser-Induced Pyrolysis and Ignition Processes of Nitramine Composite Propellants," poster presentation at 22nd Symposium (Int'l) on Combustion, Seattle, WA, August 1988.
7. Goss, L. P., and Smith, A. A., Application of Atomic Fluorescence to Measurement of Combustion Temperature in Solid Propellants, final report on AFOSR contract F49620-83-C-0138, Dec. 1986.
8. Eckbreth, A. C., Laser Diagnostics for Combustion Temperature and Species, Abacus Press, 1988.
9. Zizak, G., Omenetto, N., and Winefordner, J. D., "Laser-excited atomic fluorescence techniques for temperature measurements in flames: a summary," Optical Engineering, Vol. 23, No. 6, pp. 749-755, 1984.
10. Zizak, G., and Winefordner, J. D., "Application of the Thermally Assisted Atomic Fluorescence Technique to the Temperature Measurement in a Gasoline-Air Flame," Combustion and Flame, Vol. 44, pp. 35-41, 1982.
11. Campbell, D. H., Hulsizer, S., Edwards, T. and Weaver, D. P., "High Pressure Solid Propellant Combustion Zone Structure from Analysis of Hydroxyl Radical Chemiluminescence," Journal of Propulsion and Power, Vol. 2, No. 5, pp. 414-422, 1986.
12. Edwards, T., Solid Propellant Flame Spectroscopy, AFAL-TR-88-076, Air Force Astronautics Laboratory, Edwards AFB, CA, August 1988.

13. Parr, T. and Hanson-Parr, D., "Species and Temperature Profiles in Ignition and Deflagration of HMX," Western States Section/Combustion Institute Paper WSS/CI 87-8, April 1987. Also, "The Application of Imaging Laser-Induced Fluorescence to the Measurement of HMX and Aluminized Propellant Ignition and Deflagration Flame Structure," 23rd JANNAF Combustion Meeting, CPIA Pub. 457, Volume I, 249-267 (1986). Also, "Temperature and Species Profiles in Propellant Ignition and Combustion," 24th JANNAF Combustion Meeting, CPIA Pub. 476, Volume I, 367-382 (1987).
14. Stufflebeam, J. H., and Eckbreth, A. C., "CARS Measurements in High Pressure Solid Propellant Flames," paper presented at 25th JANNAF Combustion Meeting, Huntsville, AL, October 1988.
15. Summerfield, M., Sutherland, G. S., Webb, M. J., Taback, H. J., and Hall, K. P., "Burning Mechanism of Ammonium Perchlorate Propellants," ARS Progress in Astronautics and Rocketry Series, Volume 1: Solid Propellant Rocket Research, edited by M. Summerfield, Academic Press, Inc., New York, 1960, pp. 141-182.
16. Powling, J., and Smith, W. A. W., "Measurement of the Burning Surface Temperatures of Propellant Compositions by Infra-Red Emission," Combustion and Flame, Vol. 6, pp. 173-181, Sep. 1962.
17. Edwards, T., Weaver, D. P., Campbell, D. H., and Hulsizer, S., "A High Pressure Combustor for the Spectroscopic Study of Solid Propellant Combustion Chemistry," Review of Scientific Instruments, Vol. 56, No. 11, pp. 2131-2137, 1985.
18. Edwards, T., Weaver, D. P., and Campbell, D. H., "Laser-Induced Fluorescence in High Pressure Solid Propellant Flames," Applied Optics, Vol. 26, No. 17, pp. 3496-3509, 1987.
19. Lucht, R. P., Sweeney, D. W., and Laurendeau, N. M., "Laser-Saturated Fluorescence Measurements of OH in Atmospheric Pressure  $\text{CH}_4/\text{O}_2/\text{N}_2$  Flames Under Sooting and Non-Sooting Conditions," Combustion Science and Technology, Vol. 42, pp. 259-281, 1985.
20. Gaydon, A. G., The Spectroscopy of Flames, 2nd Edition, Chapman and Hall, London, 1974.
21. Gaydon, A. G., and Wolfhard, H. G., Flames: Their Structure, Radiation, and Temperature, 4th Edition, Chapman and Hall, London, 1979.
22. Anderson, W. R., Decker, L. J., and Kotlar, A. J., "Temperature Profile of a Stoichiometric  $\text{CH}_4/\text{N}_2\text{O}$  Flame from Laser Excited Fluorescence Measurements on OH," Combustion and Flame, Vol. 48, pp. 163-176 (1982).
23. Campbell, D. H., "Vibrational Level Relaxation Effects on Laser Induced Fluorescence Measurements of Hydroxide Number Density in a Methane-Air Flame," Applied Optics, Vol. 21, No. 16, pp. 2912-2919, 1982.

24. Campbell, D. H., "Collisional effects on laser-induced fluorescence measurements of hydroxide concentrations in a combustion environment. 1: Effects for  $v'=0$  excitation," Applied Optics, Vol. 23, No. 5, pp.689-703, 1984.
25. Campbell, D. H., "Collisional effects on laser-induced fluorescence measurements of hydroxide concentrations in a combustion environment. 2: Effects for  $v'=1$  excitation," Applied Optics, Vol. 23, No. 9, pp. 1319-1327, 1984.
26. Campbell, D. H., "Self-Absorption Effects in Emission and Laser-Induced Fluorescence Diagnostics," Paper presented at Fall 1985 Western States Section/Combustion Institute Meeting, Davis, CA, Paper WSS/CI 85-14, Oct. 1985.
27. Crosley, D. R., "Collisional effects on laser-induced fluorescence flame measurements," Optical Engineering, Vol. 20, No. 4, pp. 511-521, 1981.
28. Crosley, D.R., and Smith, G. P., "Rotational Energy Transfer and LIF Temperature Measurements," Combustion and Flame, Vol. 44, pp. 27-34, 1982.
29. Crosley, D. R., and Smith, G. P., "Vibrational energy transfer in laser-excited  $A^2\Sigma^+ OH$  as a flame thermometer," Applied Optics, Vol. 19, No. 4, pp. 517-520, 1980.
30. Smith, G. P., and Crosley, D. R., "Quantitative Laser-Induced Fluorescence in OH: Transition Probabilities and the Influence of Energy Transfer," 18th Symposium (Int'l) on Combustion, Combustion Institute, Pittsburgh, 1983, pp. 1428-1430.
31. Smith, G. P., and Crosley, D. R., "Vibrational energy transfer in  $A^2\Sigma^+ OH$  in flames," Applied Optics, Vol. 22, No. 10, pp. 517-520, 1980.
32. Copeland, R. A., and Crosley, D. R., "Rotational-level-dependent quenching of  $A^2\Sigma^+ OH$  and OD," Journal of Chemical Physics, Vol. 82, No. 9, pp. 4022-4032, 1985.
33. Kohse-Hoinghaus, K., Jeffries, J. B., Copeland, R. A., Smith, G. P., and Crosley, D. R., "The Quantitative LIF Determination of OH Concentration in Low-Pressure Flames," paper presented at the 22nd Symposium (Int'l) on Combustion, Seattle, WA, August 1988.
34. Cattolica, R., "OH rotational temperature from two-line laser-excited fluorescence," Applied Optics, Vol. 20, No. 7, pp. 1156-1166, 1981.
35. Lucht, R. P., Laurendeau, N. M., and Sweeney, D. W., "Temperature measurement by two-line laser-saturated OH fluorescence in flames," Applied Optics, Volume 21, No. 20, pp. 3729-3735, 1982.
36. Laurendeau, N. M., and Goldsmith, J. E. M., "Comparison of Laser-Induced Fluorescence Methods for Measurement of Hydroxyl Concentration in Flames," Western States Section/Combustion Institute Paper WSS/CI 86-27, April 1986.

37. Carter, C. D., Salmon, J. T., King, G. B., and Laurendeau, N. M., "Feasibility of hydroxyl concentration measurements by laser-saturated fluorescence in high-pressure flames," Applied Optics, Vol. 26, No. 21, pp. 4551-4562, 1987
38. Gross, K. P., and McKenzie, R. L., "Single-pulse gas thermometry at low temperatures using two-photon laser-induced fluorescence in NO-N<sub>2</sub> mixtures," Optics Letters, Vol. 8, No. 7, pp. 368-370, 1983.
39. Dieke, G. H., and Crosswhite, H. M., "The Ultraviolet Bands of OH," Journal of Quantitative Spectroscopy and Radiative Transfer, Vol. 2, pp. 97-199, 1962.
41. Chidsey, I. L., and Crosley, D. R., "Calculated Rotational Transition Probabilities for the A-X System of OH," Journal of Quantitative Spectroscopy and Radiative Transfer, Vol. 23, pp. 187-199, 1980.
42. Garland, N. L., and Crosley, D. R., "On the Collisional Quenching of Electronically Excited OH, NH, and CH in Flames," 21st Symposium (Int'l) on Combustion, Combustion Institute, Pittsburgh, 1988, pp.1693-1702.
43. Smith, G. P., and Crosley, D. R., "Quenching of OH ( $A^2\Sigma^+$ ,  $v'=0$ ) by H<sub>2</sub>, N<sub>2</sub>O, and hydrocarbons at elevated temperatures," Journal of Chemical Physics, Vol. 85, No. 7, pp. 3896-3901, 1986.
44. Fairchild, P. W., Smith, G. P., and Crosley, D. R., "Collisional quenching of  $A^2\Sigma^+$  OH at elevated temperatures," Journal of Chemical Physics, Vol. 79, No. 4, pp. 1795-1807, 1983.
45. Zabarnick, S., Fleming, J. W., and Baronavski, A. P., "Production of OH from the collision-free photodissociation of nitromethane," Journal of Chemical Physics, Vol. 85, No. 6, pp. 3395-3400, 1986.
46. Glassman, I., "Soot Formation in Combustion Processes," paper presented at 22nd Symposium (Int'l) on Combustion, Seattle, WA, August 1988.
47. Jain, S. R., "Energetics of Propellants, Fuels and Explosives," Propellants, Explosives, Pyrotechnics, Vol. 12, 188-195, 1987.
48. Coxon, J. A., "Optimum Molecular Constants and Term Values for the  $X^2\Pi$  ( $v\leq 5$ ) and  $A^2\Sigma^+$  ( $v\leq 3$ ) States of OH," Canadian Journal of Physics, Vol. 58, 933-949 (1980).
49. Anderson, W. R., Decker, L. J., and Kotlar, A. J., "Concentration Profiles of NH and OH in a Stoichiometric CH<sub>4</sub>/N<sub>2</sub>O Flame by Laser-Excited Fluorescence and Absorption," Combustion and Flame, Vol. 48, pp. 179-190, 1982.

50. Jeffries, J. B., Rensburger, K. J., Copeland, R. A., Kohse-Hoinghaus, K., Wise, M. L., and Crosley, D. , "Laser-Induced Fluorescence Determination of Temperature in Low-Pressure Flames," Paper presented at Spring 1988 Western States Section/Combustion Institute Meeting, Paper WSS/CI 88-57, 1988.
51. Chan, C., and Daily, J. W., "Measurement of temperature in flames using laser induced fluorescence spectroscopy of OH," Applied Optics, Vol. 19, No. 12, pp. 1963-1968, 1980.
52. Zizak, G., Horvath, J. J., and Winefordner, J. D., "Flame Temperature Measurement by Redistribution of Rotational Population in Laser-Excited Fluorescence: An Application to the OH Radical in a Methane-Air Flame," Applied Spectroscopy, Vol. 35, No. 5, pp. 488-493, 1981.
53. Vaidya, D. B., Horvath, J. J., and Green, A. E. S., "Remote Temperature Measurements in Gas and Gas-Coal Flames Using the OH (0,0) Middle-UV Band, Applied Optics, Vol. 21, pp. 3357-3362, 1982.
54. Jensen, R. J., and Fisher, S. C., "Nonintrusive Temperature Measurements in SSME Preburner Element Flowfields," 23rd JANNAF Combustion Meeting, Vol. I, CPIA Publication 457, pp. 633-640, 1986.

# APPENDIX A. OH SPECTROSCOPIC DATA

OH 1,1 band ID	Wavelength, nm (Ref.39)	B coefficient (Ref. 41)	J"	J'	Rotational energy, cm <sup>-1</sup> (Ref. 39)
R <sub>1</sub> 5	281.1319	169	5.5	6.5	543.54
R <sub>1</sub> 6	281.1382	179	6.5	7.5	767.45
R <sub>1</sub> 5'	281.1429	48	5.5	5.5	543.54
R <sub>1</sub> 6'	281.1507	39	6.5	6.5	767.45
R <sub>1</sub> 4	281.1591	155	4.5	5.5	355.09
R <sub>1</sub> 4'	281.1684	60	4.5	4.5	355.09
R <sub>1</sub> 7	281.1797	186	7.5	8.5	1026.69
R <sub>1</sub> 7'	281.1941	32	7.5	7.5	1026.69
R <sub>1</sub> 3	281.2162	137	3.5	4.5	201.90
R <sub>1</sub> 3'	281.2237	75	3.5	3.5	201.90
R <sub>1</sub> 8	281.2591	192	8.5	9.5	1321.25
R <sub>1</sub> 8'	281.2750	26	8.5	8.5	1321.25
R <sub>1</sub> 2	281.2984	111	2.5	3.5	83.70
R <sub>1</sub> 2'	281.3044	94	2.5	2.5	83.70
R <sub>1</sub> 9	281.3776	197	9.5	10.5	1650.74
R <sub>1</sub> 9'	281.3947	22	9.5	9.5	1650.74
R <sub>1</sub> 1	281.4005	71	1.5	2.5	0
R <sub>1</sub> 1'	281.4045	108	1.5	1.5	0
R <sub>1</sub> 10	281.5368	201	10.5	11.5	2014.98
R <sub>1</sub> 10'	281.5558	19	10.5	10.5	2014.98
R <sub>2</sub> 7	281.5989	195	6.5	7.5	1077.80
R <sub>2</sub> 6	281.6024	190	5.5	6.5	824.49
R <sub>2</sub> 8	281.6423	199	7.5	8.5	1367.56
R <sub>2</sub> 5	281.6549	183	4.5	5.5	608.15
R <sub>2</sub> 9	281.7319	203	8.5	9.5	1693.15
R <sub>1</sub> 11	281.7380	204	11.5	12.5	2413.51
R <sub>1</sub> 11''	281.7580	16	11.5	11.5	2413.51
R <sub>2</sub> 4''	281.7580	174	3.5	4.5	429.45
R <sub>2</sub> 10	281.8677	206	9.5	10.5	2054.26
Q <sub>1</sub> 1*	281.9145	240	1.5	1.5	0.03
Q <sub>1</sub> 1''	281.9145	169	1.5	0.5	0.03
R <sub>2</sub> 3*	281.9145	164	2.5	3.5	289.01
R <sub>1</sub> 12	281.9822	207	12.5	13.5	2846.01
R <sub>1</sub> 12'	282.0040	14	12.5	12.5	2846.01
R <sub>2</sub> 11	282.0501	208	10.5	11.5	2450.15
Q <sub>1</sub> 2	282.0669	303	2.5	2.5	83.90
Q <sub>1</sub> 2'	282.0710	104	2.5	1.5	83.90
R <sub>2</sub> 2	282.1302	153	1.5	2.5	187.71
P <sub>1</sub> 1	282.1706	251	1.5	0.5	0
Q <sub>1</sub> 3	282.2404	338	3.5	3.5	202.37
Q <sub>1</sub> 3'	282.2466	72	3.5	2.5	202.37
R <sub>1</sub> 13	282.2705	209	13.5	14.5	3311.83
R <sub>2</sub> 12	282.2787	210	11.5	12.5	2880.46
R <sub>1</sub> 13'	282.2953	13	13.5	13.5	3311.83
R <sub>2</sub> 1	282.4096	144	0.5	1.5	126.43



OH 1,1 band ID	Wavelength, nm (Ref. 39)	B coefficient (Ref. 41)	J"	J'	Rotational energy, cm <sup>-1</sup> (Ref. 39)
Q <sub>1</sub> 4	282.4393	361	4.5	4.5	355.87
Q <sub>1</sub> 4'	282.4455	53	4.5	3.5	355.87
R <sub>2</sub> 13	282.5545	212	12.5	13.5	3344.34
P <sub>1</sub> 2	282.5802	225	2.5	1.5	83.70
R <sub>1</sub> 14	282.6058	211	14.5	15.5	3810.60
R <sub>1</sub> 14'	282.6317	11	14.5	14.5	3810.60
Q <sub>1</sub> 5	282.6674	377	5.5	5.5	544.82
Q <sub>1</sub> 5'	282.6764	40	5.5	4.5	544.82
R <sub>2</sub> 14	282.8784	214	13.5	14.5	2841.51
Q <sub>2</sub> 2'	282.8942	103	1.5	2.5	187.47
Q <sub>2</sub> 2	282.8984	294	1.5	1.5	187.47
Q <sub>2</sub> 1*	282.9225	286	0.5	0.5	126.12
Q <sub>2</sub> 1**	282.9225	144	0.5	1.5	126.12
Q <sub>1</sub> 6*	282.9277	388	6.5	6.5	769.17
Q <sub>2</sub> 3**	282.9277	76	2.5	3.5	288.83
Q <sub>1</sub> 6**	282.9373	31	6.5	5.5	769.17
Q <sub>2</sub> 3*	282.9373	323	2.5	2.5	288.83
R <sub>1</sub> 15	282.9879	212	15.5	16.5	4341.70
P <sub>1</sub> 3	283.0095	218	3.5	2.5	201.90
Q <sub>2</sub> 4'	283.0257	58	3.5	4.5	429.23
Q <sub>2</sub> 4	283.0339	348	3.5	3.5	429.23
Q <sub>2</sub> 5'	283.1748	45	4.5	5.5	608.16
Q <sub>2</sub> 5*	283.1838	366	4.5	4.5	608.16
P <sub>2</sub> 1**	283.1838	286	0.5	0.5	126.43
Q <sub>1</sub> 7	283.2222	397	7.5	7.5	1029.10
Q <sub>1</sub> 7'	283.2351	25	7.5	6.5	1029.10
R <sub>2</sub> 15	283.2512	215	14.5	15.5	4371.18
Q <sub>2</sub> 6'	283.3731	35	5.5	6.5	824.76
Q <sub>2</sub> 6	283.3843	379	5.5	5.5	824.76
P <sub>2</sub> 2'	283.4143	161	1.5	1.5	187.71
R <sub>1</sub> 16*	283.4172	213	16.5	17.5	4904.53
P <sub>2</sub> 2*	283.4172	116	1.5	0.5	187.71
P <sub>1</sub> 4	283.4630	215	4.5	3.5	355.09
Q <sub>1</sub> 8	283.5530	403	8.5	8.5	1324.24
Q <sub>1</sub> 8'	283.5675	20	8.5	7.5	1324.24
Q <sub>2</sub> 7'	283.6189	28	6.5	7.5	1078.47
Q <sub>2</sub> 7	283.6320	389	6.5	6.5	1078.47
R <sub>2</sub> 16*	283.6736	215	15.5	16.5	4932.80
Q <sub>2</sub> 2*	283.6736	34	1.5	0.5	187.47
P <sub>2</sub> 3'	283.7094	115	2.5	2.5	289.01
P <sub>2</sub> 3	283.7134	150	2.5	1.5	289.01
R <sub>1</sub> 17	283.8984	213	17.5	18.5	5498.27
Q <sub>2</sub> 8'	283.9108	23	7.5	8.5	1368.66
Q <sub>1</sub> 9*	283.9234	407	9.5	9.5	1654.50
Q <sub>2</sub> 8*	283.9234	397	7.5	7.5	1368.66
Q <sub>1</sub> 9'	283.9378	16	9.5	8.5	1654.50
P <sub>1</sub> 5	283.9450	214	5.5	4.5	543.54

OH 1,1 band ID	Wavelength, nm (Ref.39)	B coefficient (Ref. 41)	J"	J'	Rotational energy, cm <sup>-1</sup> (Ref. 39)
P <sub>2</sub> 4'	284.0621	86	3.5	3.5	429.45
P <sub>2</sub> 4	284.0681	169	3.5	2.5	429.45
R <sub>2</sub> 17	284.1481	216	16.5	17.5	5525.50
O <sub>2</sub> 3	284.2282	30	2.5	1.5	288.83
Q <sub>2</sub> 9'	284.2471	19	8.5	9.5	1694.85
Q <sub>2</sub> 9	284.2635	402	8.5	8.5	1694.85
Q <sub>1</sub> 10	284.3294	411	10.5	10.5	2019.53
Q <sub>1</sub> 10'	284.3470	14	10.5	9.5	2019.53
R <sub>1</sub> 18	284.4304	214	18.5	19.5	6122.51
P <sub>1</sub> 6	284.4581	213	6.5	5.5	767.45
P <sub>2</sub> 5'	284.4670	66	4.5	4.5	608.15
P <sub>2</sub> 5	284.4750	181	4.5	3.5	608.15
Q <sub>2</sub> 10'	284.6280	16	9.5	10.5	2056.46
Q <sub>2</sub> 10	284.6461	407	9.5	9.5	2056.46
R <sub>2</sub> 18	284.6741	216	17.5	18.5	6148.33
Q <sub>1</sub> 11	284.7771	413	11.5	11.5	2419.05
Q <sub>1</sub> 11'	284.7967	12	11.5	10.5	2419.05
O <sub>2</sub> 4	284.8429	24	3.5	2.5	429.23
P <sub>2</sub> 6'	284.9206	52	5.5	5.5	824.49
P <sub>2</sub> 6	284.9304	188	5.5	4.5	824.49
P <sub>1</sub> 7	285.0046	212	7.5	6.5	1026.69

\* Overlapped by nearby lines and thus not usable. The rotational energy refers to the lower state (v").

## APPENDIX B. OH SPECTRAL FITTING PROGRAM

As a part of this effort, a program to create "synthetic" OH spectra was constructed. This is a limited effort compared to the program created by Campbell (Ref. 11), who included such effects as self-absorption and a fitting routine to simulate OH emission spectra from high pressure solid propellant flames.

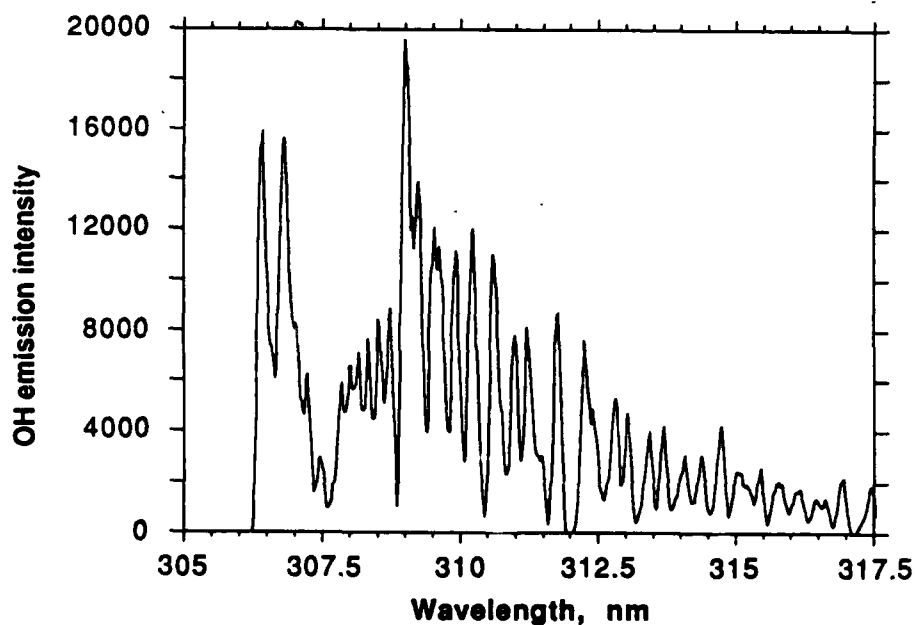
The program calculates the line locations and intensities of the 12 branches of the OH  $A^2\Sigma - X^2\Pi$  system. The branches are listed in Table 2. The line locations were originally calculated using the standard spectroscopic equations for the OH transition terms, e.g.,

$$F_1(v,N) = B_v(v) * N * (N+1) - D_v(v) * N^2 * (N+1)^2 + R * (N+0.5) + \text{vibrational terms.}$$

However, this yielded unsatisfactory results for the line locations, so tabular values for the terms were used in the program (Ref. 39,48). Then the wavenumber of the line was calculated as the differences of the terms, as shown in the table. The relative intensity of a given line was calculated as  $E(v,N) = A * g * BF * BG$ ; where  $A$  is the Einstein coefficient for stimulated emission;  $g$  is the degeneracy ( $2J+1$ );  $BF$  is the rotational Boltzmann factor ( $BF = \exp(-hcF/kT_r)$ ); and  $BG$  is the vibrational Boltzmann factor ( $BG = \exp(-hcG/kT_v)$ ). The Einstein coefficients and vibrational terms were taken from tables (Ref. 41,39). The vibrational and rotational temperatures ( $T_v$  and  $T_r$ , respectively) were inputs to the program. When the lines and intensities were calculated, the program "scanned" a triangular slit function over the lines to approximate the experimental data taken with spectrometers. For this initial program, the width of the lines was assumed to be very small compared to the slit function, with the lines treated as delta functions at the line center. The width (FWHM) of the slit function, the number of steps in the "scan," and the incremental distance between steps were inputs to the program. To model emission spectra or some aspects of the LIF spectra, the values of  $A$ ,  $g$ ,  $BF$ , and  $BG$  were calculated for the excited state ( $A^2\Sigma$ ). For example, a synthetic OH emission spectrum with  $T_v = T_r = 2500$  K is shown in Figure 44. The scanning parameters were selected to simulate emission spectra taken with a Reticon diode array detector (e.g., Figure 18). The slit function has a FWHM width of 0.125 nm, 1500 data points, with 0.0175 nm between points starting at 305 nm. The match between experimental and synthetic spectra is fairly good. To simulate a low pressure LIF spectrum where there is little collisional redistribution before radiation, the program could be constrained to examine only lines directly coupled to the laser line. An example of such a calculation is shown in Figure 45. It is obvious by comparing Figures 45 and 2 that a great deal of rotational and vibrational redistribution is occurring. If one assumes total rotational thermalization and limited vibrational thermalization, the OH model spectrum shown in Figure 46 is obtained. It is apparent from this that the LIF spectrum of Figure 2 is partly thermalized by collisions. Detailed models of flame LIF experiments can be used to calculate a temperature from a spectrum similar to Figure 2 (Ref. 51,52), although the models are complex and the detailed rate data needed is not totally reliable.

Table. OH model data

Transition	N'	J''	J'
<b>Main branches</b>			
$P_1=F_1(N')-f_1(N'')$	$N''-1$	$N''+0.5$	$J''-1=N''-0.5=N'+0.5$
$P_2=F_2(N')-f_2(N'')$	$N''-1$	$N''-0.5$	$J''-1=N''-1.5=N'-0.5$
$Q_1=F_1(N')-f_1'(N'')$	$N''$	$N''+0.5$	$J''=N''+0.5=N'+0.5$
$Q_2=F_2(N')-f_2'(N'')$	$N''$	$N''-0.5$	$J''=N''-0.5=N'-0.5$
$R_1=F_1(N')-f_1(N'')$	$N''+1$	$N''+0.5$	$J''+1=N''+1.5=N'+0.5$
$R_2=F_2(N')-f_2(N'')$	$N''+1$	$N''-0.5$	$J''+1=N''+0.5=N'-0.5$
<b>Satellite transitions</b>			
$O_{12}=O_2=F_1(N')-f_2'(N'')$	$N''-2$	$N''-0.5$	$J''-1=N''-1.5=N'+0.5$
$P_{12}=P_2'=F_1(N')-f_2(N'')$	$N''-1$	$N''-0.5$	$J''=N''-0.5=N'+0.5$
$Q_{12}=Q_2'=F_1(N')-f_2'(N'')$	$N''$	$N''-0.5$	$J''+1=N''+0.5=N'+0.5$
$Q_{21}=Q_1'=F_2(N')-f_1'(N'')$	$N''$	$N''+0.5$	$J''-1=N''-0.5=N'-0.5$
$R_{21}=R_1'=F_2(N')-f_1(N'')$	$N''+1$	$N''+0.5$	$J''=N''+0.5=N'-0.5$
$S_{21}=S_1=F_2(N')-f_1'(N'')$	$N''+2$	$N''+0.5$	$J''+1=N''+1.5=N'-0.5$

Figure 44. OH model spectrum.  $T_v=T_r=2500$  K.

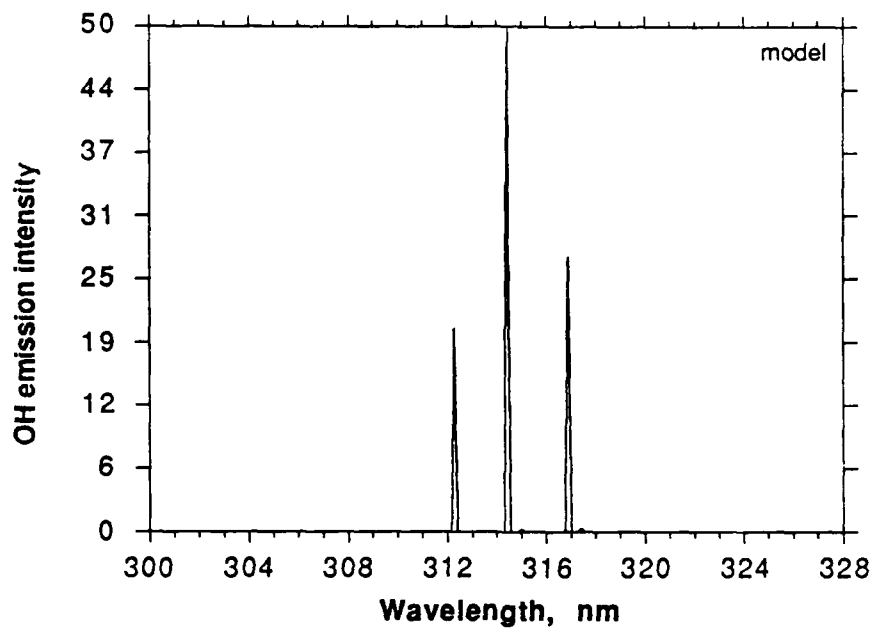


Figure 46. OH model spectrum. Lines directly coupled to OH 1,0 R<sub>1</sub> 5. Lines are 1,1 R<sub>1</sub> 5, Q<sub>1</sub> 6, Q<sub>12</sub> 6 (weak), P<sub>1</sub> 7, and P<sub>12</sub> 7 (very weak).

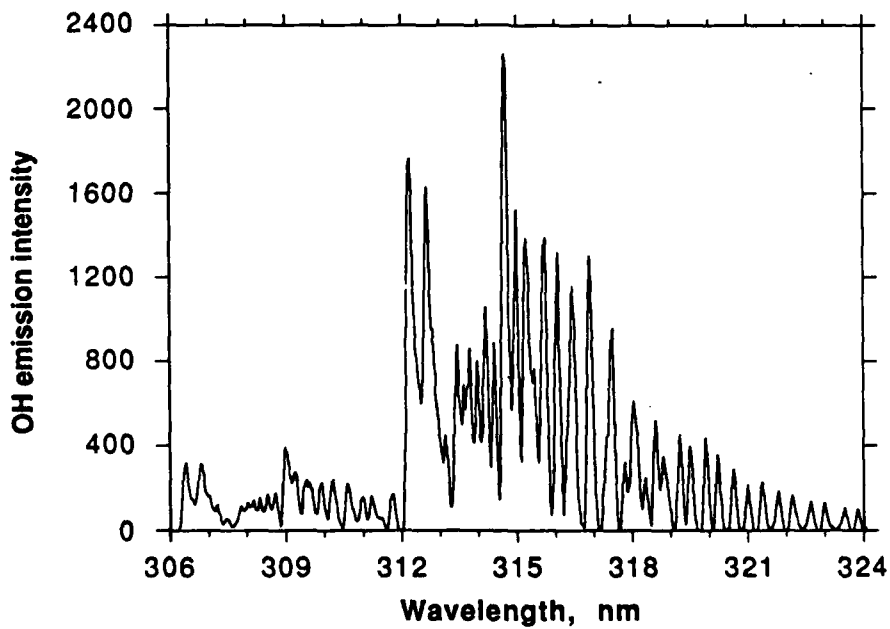


Figure 47. OH model spectrum. Same as Figure 44 but 0,0 A coefficients divided by 50.

Program listing: (run on Macintosh computer using Absoft Fortran Compiler Version 2.3)

```

PROGRAM BOLTZM
C
C CALCULATES SYNTHETIC SPECTRA IN MOLECULE
C AS A FUNCTION OF TEMPERATURE. CURRENTLY ONLY FOR
C 0,0 AND 1,1 BANDS. BASED ON BOLTZMANN DISTRIBUTION.
C ALLOW FOR V=1-4 AND N=1-40.
C
  DIMENSION VZERO(4,4),G1(5),G2(5)
  DIMENSION ENET(2000),EINCR(2000),WSCAN(2000),ESUM(2000)
  DIMENSION F11(4,40),F12(4,40),F21(4,40),F22(4,40)
  DIMENSION VP1(4,40),VP2(4,40),VQ1(4,40),VQ2(4,40)
  DIMENSION VQ12(4,40),VQ21(4,40),VR21(4,40),VP12(4,40)
  DIMENSION VR1(4,40),VR2(4,40)
  DIMENSION F21P(4,40),B1(4),F22P(4,40)
  DIMENSION BF1(4,40),BF2(4,40),BG(4)
  DIMENSION ENR1(4,40),ENR2(4,40),ENQ1(4,40),ENQ2(4,40)
  DIMENSION ENP1(4,40),ENP2(4,40),ENR21(4,40),ENP12(4,40)
  DIMENSION ENQ12(4,40),ENQ21(4,40)
  DIMENSION WAVQ1(4,40),WAVQ2(4,40),WAVP1(4,40)
  DIMENSION WAVP2(4,40),WAVR1(4,40),WAVR2(4,40)
  DIMENSION WAVR21(4,40),WAVP12(4,40),WAVQ12(4,40),WAVQ21(4,40)
  DIMENSION ASPP1(4,40),ASPP2(4,40),ASPO1(4,40)
  DIMENSION ASPQ2(4,40),ASPR1(4,40),ASPR2(4,40)
  DIMENSION ASPQ12(4,40),ASPQ21(4,40),ASPR21(4,40),ASPP12(4,40)
  DIMENSION GR1(25),GR2(25),GQ1(25),GQ2(25),GP1(25),GP2(25)
  DIMENSION GP12(25),GR21(25),GQ12(25),GQ21(25)
  DIMENSION GO12(25),GS21(25)
  INTEGER*2 N,COLUMNS
  INTEGER*2 NDATA,DELTIV
C
  OPEN(UNIT=23, FILE='OH START', FORM='FORMATTED', STATUS='OLD')
  READ (23,250) TROT,TVIB,WINIT,RES,WINCR,NDATA,DELTIV
250  FORMAT(3F9.3,F6.3,F6.4,I5,I4)
C
C CAN WRITE MOLECULE INFO IF DESIRED
C
  WRITE(9,300)
300  FORMAT ('MOLECULE IS OH')
  WRITE(9,400) TROT,TVIB
400  FORMAT ('BOLTZMANN DISTRIBUTION FOR TROT,TVIB=',F9.3,',',F9.3)
  WRITE(9,450) WINIT,RES,WINCR,NDATA,DELTIV
450  FORMAT('WINIT=',F9.3,5X,'RES=',F6.3,5X,'WINCR=',F6.4,/,
1    'NDATA=',I4,5X,'DELTIV=',I4)
  CLOSE(UNIT=23)
  OPEN(UNIT=23, FILE='OH LINES', FORM='FORMATTED', STATUS='NEW')
C
C
C NOTE!!!!!! NEED DUMMY VARIABLES SINCE ARRAYS CANT HAVE ZEROS!
C SO NV1=NV2=1 FOR 0,0 BAND, ETC, AND N1=0, SO USE N1 IN CALCS
C
C NEED DATA FOR EINSTEIN A COEFFICIENTS FOR SPONTANEOUS
C EMISSION (ASP**(NV1,N)=A COEFF FOR BRANCH **)
C FROM CHIDSEY AND CROSLY (JQSRT 23:187-199 (1980))
C
  ASPP1(1,1)=1000

```

```

      ASPP1(1,2)=671
      ...
      (data omitted to save paper)
      ...
      ASPR2(2,27)=60
      ASPR2(2,28)=53
C
C   DATA FROM HUBER AND HERZBERG
C   T=ELECTRONIC TERM FOR OH A STATE
C
      T1=32684.1
C
C   DATA FROM DIEKE AND CROSSWHITE
C   FOR G(V)=VIBRATIONAL (ROTATIONLESS) TERM ENERGY
C   G1=G' (A STATE), G2=G'' (GROUND STATE)
C
      G1(1)=1567.68
      G1(2)=G1(1)+2988.60
      G1(3)=G1(2)+2792.92
      G1(4)=G1(3)+2593.36
      G2(1)=1847.052
      G2(2)=G2(1)+3569.59
      G2(3)=G2(2)+3403.97
C
C
C
      DO 2600 NV1=1,2
C
C   HERE IS WHERE THE BAND SEQUENCES ARE INPUT--0,0->NV1=NV2--
C   THUS DELTV=0,+1,-1 FOR 0,0;0,1; AND THE 1,0 SEQUENCES
C   NV2=NV1-DELTV
C
C
      VZERO(NV1,NV2)=T1+G1(NV1)-G2(NV2)
C
C   N1,N2 ARE ACTUAL N
C
      N1=NV1-1
      N2=NV2-1
C
C
      WRITE(9,350) N1,N2
350  FORMAT (/, 'CALCULATING', 3X, I3, ', ', I3, 3X, 'LINES')
      WRITE(23,375) N1,N2
375  FORMAT (/, 'BAND IS', I3, ', ', I3)
C
C   VIBRATIONAL BOLTZMANN FACTOR=BG(NV1)
C   hc/k=1.43836 [K/WAVENUMBER]
C
      BG(NV1)=EXP(-1.43836*G1(NV1)/TVIB)
C
C   DATA INPUT FORMAT F2=f, F1=F
C   F21=f1 COMPONENT, F21P=f1', ETC., FUNCTION OF N AND V
C   F(N,NV) LISTED BELOW. F AND f IN TABLES INCLUDES
C   VIBRATIONAL AND ELECTRONIC ENERGY
C
      F11(1,1)=32474.62
      F11(1,2)=32542.56

```

```

...
(data omitted to save paper)
...
      F22P(2,27)=16069.01
      F22P(2,28)=16915.75
C
      DO 2500 N=1,25
C
C      N=N", NP=N' FOR P BRANCH, ETC.
C
      NP=N-1
      NR=N+1
      NQ=N
      NO=N-2
      NS=N+2
C
C      G=DEGENERACY=2J'+1 IN EMISSION
C
      GR1(N)=2*(N+1.5)+1
      GR2(N)=2*(N+0.5)+1
      GQ1(N)=2*(N+0.5)+1
      GQ2(N)=2*(N-0.5)+1
      GP1(N)=2*(N-0.5)+1
      GP2(N)=2*(N-1.5)+1
      GO12(N)=2*(N-2.5)+1
      GP12(N)=2*(N-1.5)+1
      GQ12(N)=2*(N-0.5)+1
      GQ21(N)=2*(N+0.5)+1
      GR21(N)=2*(N+1.5)+1
      GS21(N)=2*(N+2.5)+1
C
      IF(NP.EQ.0) GO TO 650
C
      VP1(NV1,N)=F11(NV1,NP)-F21(NV2,N)
      VP2(NV1,N)=F12(NV1,NP)-F22(NV2,N)
      VP12(NV1,N)=F11(NV1,NP)-F22(NV2,N)
C
C      INPUT DATA FOR 0,0 AND 1,1 BANDS FOR P1 AND P2, N=1
C
650      VP1(1,1)=32440.60
      VP2(1,1)=0
      VP1(2,1)=31860.78
      VP2(2,1)=0
      VP12(1,1)=32314.19
      VP12(2,1)=31733.71
C
C      IGNORE O AND S BRANCHES FOR NOW
C
      VQ1(NV1,N)=F11(NV1,NQ)-F21P(NV2,N)
      VQ2(NV1,N)=F12(NV1,NQ)-F22P(NV2,N)
      VR1(NV1,N)=F11(NV1,NR)-F21(NV2,N)
      VR2(NV1,N)=F12(NV1,NR)-F22(NV2,N)
      VQ12(NV1,N)=F11(NV1,NQ)-F22P(NV2,N)
      VQ21(NV1,N)=F12(NV1,NQ)-F21P(NV2,N)
      VR21(NV1,N)=F12(NV1,NR)-F21(NV2,N)
C
C      BF=ROTATIONAL BOLTZMANN FACTOR
C      SUBTRACT VIBRATIONAL ENERGY TO OBTAIN ROTATION ONLY

```



```

C      BF1 (NV1,N)=EXP (-1*1.43836* (F11 (NV1,N)-T1-G1 (NV1)) /TROT)
      BF2 (NV1,N)=EXP (-1*1.43836* (F12 (NV1,N)-T1-G1 (NV1)) /TROT)
C
      ENR1 (NV1,N)=ASPR1 (NV1,N)*BF1 (NV1,N)*BG (NV1)*GR1 (N)
      ENR2 (NV1,N)=ASPR2 (NV1,N)*BF2 (NV1,N)*BG (NV1)*GR2 (N)
      WAVR1 (NV1,N)=1.0E07/ (VR1 (NV1,N)*1.00029)
      WAVR2 (NV1,N)=1.0E07/ (VR2 (NV1,N)*1.00029)
C
      ENQ1 (NV1,N)=ASPQ1 (NV1,N)*BF1 (NV1,N)*BG (NV1)*GQ1 (N)
      ENQ2 (NV1,N)=ASPQ2 (NV1,N)*BF2 (NV1,N)*BG (NV1)*GQ2 (N)
      WAVQ1 (NV1,N)=1.0E07/ (VQ1 (NV1,N)*1.00029)
      WAVQ2 (NV1,N)=1.0E07/ (VQ2 (NV1,N)*1.00029)
C
      ENP12 (NV1,N)=ASPP12 (NV1,N)*BF1 (NV1,N)*BG (NV1)*GP12 (N)
      ENR21 (NV1,N)=ASPR21 (NV1,N)*BF2 (NV1,N)*BG (NV1)*GR21 (N)
      WAVP12 (NV1,N)=1.0E07/ (VP12 (NV1,N)*1.00029)
      WAVR21 (NV1,N)=1.0E07/ (VR21 (NV1,N)*1.00029)
C
      ENQ12 (NV1,N)=ASPQ12 (NV1,N)*BF1 (NV1,N)*BG (NV1)*GQ12 (N)
      ENQ21 (NV1,N)=ASPQ21 (NV1,N)*BF2 (NV1,N)*BG (NV1)*GQ21 (N)
      WAVQ12 (NV1,N)=1.0E07/ (VQ12 (NV1,N)*1.00029)
      WAVQ21 (NV1,N)=1.0E07/ (VQ21 (NV1,N)*1.00029)
C
      ENP1 (NV1,N)=ASPP1 (NV1,N)*BF1 (NV1,N)*BG (NV1)*GP1 (N)
      ENP2 (NV1,N)=ASPP2 (NV1,N)*BF2 (NV1,N)*BG (NV1)*GP2 (N)
C
      IF (VP1 (NV1,N).EQ.0.0) GO TO 890
      IF (VP2 (NV1,N).EQ.0.0) GO TO 890
C
      WAVP1 (NV1,N)=1.0E07/ (VP1 (NV1,N)*1.00029)
      WAVP2 (NV1,N)=1.0E07/ (VP2 (NV1,N)*1.00029)
C
890    CONTINUE
C
      WRITE (23,895) N,VR1 (NV1,N),ENR1 (NV1,N),VR2 (NV1,N),
1      ENR2 (NV1,N)
895    FORMAT ('N=',I2,1X,'VR1=',F10.4,2X,'ENR1=',F10.4,2X,
1      'VR2=',F10.4,2X,'ENR2=',F10.4)
      WRITE (23,896) N,VQ1 (NV1,N),ENQ1 (NV1,N),VQ2 (NV1,N),
1      ENQ2 (NV1,N)
896    FORMAT ('N=',I2,1X,'VQ1=',F10.4,2X,'ENQ1=',F10.4,2X,
1      'VQ2=',F10.4,2X,'ENQ2=',F10.4)
      WRITE (23,897) N,VP1 (NV1,N),ENP1 (NV1,N),VP2 (NV1,N),
1      ENP2 (NV1,N)
897    FORMAT ('N=',I2,1X,'VP1=',F10.4,2X,'ENP1=',F10.4,2X,
1      'VP2=',F10.4,2X,'ENP2=',F10.4)
      WRITE (23,898) N,VR21 (NV1,N),ENR21 (NV1,N),VP12 (NV1,N),
1      ENP12 (NV1,N)
898    FORMAT ('N=',I2,1X,'VR21=',F10.4,2X,'ENR21=',F10.4,2X,
1      'VP12=',F10.4,2X,'ENP12=',F10.4)
      WRITE (23,899) N,VQ12 (NV1,N),ENQ12 (NV1,N),VQ21 (NV1,N),
1      ENQ21 (NV1,N)
899    FORMAT ('N=',I2,1X,'VQ12=',F10.4,2X,'ENQ12=',F10.4,2X,
1      'VQ21=',F10.4,2X,'ENQ21=',F10.4)
C
C

```

```

2500  CONTINUE
2600  CONTINUE
      WRITE (9,2700)
2700  FORMAT (/, 'LINE CALCULATIONS COMPLETE - SCANNING UNDERWAY',/)
      CLOSE (UNIT=23)
      OPEN(UNIT=23, FILE='DATA', FORM='FORMATTED', STATUS='NEW')
C
C    NOW START SCANNING OVER LINES
C
      DO 3000 I=1, NDATA
3000  WSCAN(I)=0.000
      WSCAN(0)=WINIT
      DO 8000 L=1, NDATA
      DO 3100 I2=1, NDATA
3100  EINCR(I2)=0.000
      DO 3200 I3=1, NDATA
3200  ENET(I3)=0.000
      M=L-1
      WSCAN(L)=WSCAN(M)+WINCR
C
C    NOW FOR R LOOPS
C
      DO 6700 NV1=1, 2
C
      DO 4000 N=1, 25
      WDELTA=WSCAN(L)-WAVR1(NV1,N)
      DELTA=ABS(WDELTA)
      IF (DELTA.GT.RES) GO TO 3900
      FRAC=(RES-DELTA)/RES
      GO TO 3950
3900  FRAC=0.000
3950  EINCR(N)=FRAC*ENR1(NV1,N)
      ENET(L)=ENET(L)+EINCR(N)
4000  CONTINUE
      DO 4100 N=1, 25
      WDELTA=WSCAN(L)-WAVR2(NV1,N)
      DELTA=ABS(WDELTA)
      IF (DELTA.GT.RES) GO TO 4025
      FRAC=(RES-DELTA)/RES
      GO TO 4050
4025  FRAC=0.000
4050  EINCR(N)=FRAC*ENR2(NV1,N)
      ENET(L)=ENET(L)+EINCR(N)
4100  CONTINUE
C
C    NOW FOR P LOOPS
C
      DO 4250 N=1, 25
      WDELTA=WSCAN(L)-WAVP1(NV1,N)
      DELTA=ABS(WDELTA)
      IF (DELTA.GT.RES) GO TO 4220
      FRAC=(RES-DELTA)/RES
      GO TO 4225
4220  FRAC=0.000
4225  EINCR(N)=FRAC*ENP1(NV1,N)
      ENET(L)=ENET(L)+EINCR(N)
4250  CONTINUE
      DO 4300 N=1, 25

```

```

WDELTA=WSCAN(L)-WAVP2(NV1,N)
DELTA=ABS(WDELTA)
IF(DELTA.GT.RES) GO TO 4275
FRAC=(RES-DELTA)/RES
GO TO 4280
4275 FRAC=0.000
4280 EINCR(N)=FRAC*ENP2(NV1,N)
      ENET(L)=ENET(L)+EINCR(N)
4300 CONTINUE
C
C   NOW FOR Q LOOPS
C
      DO 4500 N=1,25
      WDELTA=WSCAN(L)-WAVQ1(NV1,N)
      DELTA=ABS(WDELTA)
      IF(DELTA.GT.RES) GO TO 4425
      FRAC=(RES-DELTA)/RES
      GO TO 4450
4425 FRAC=0.000
4450 EINCR(N)=FRAC*ENQ1(NV1,N)
      ENET(L)=ENET(L)+EINCR(N)
4500 CONTINUE
      DO 4600 N=1,25
      WDELTA=WSCAN(L)-WAVQ2(NV1,N)
      DELTA=ABS(WDELTA)
      IF(DELTA.GT.RES) GO TO 4525
      FRAC=(RES-DELTA)/RES
      GO TO 4550
4525 FRAC=0.000
4550 EINCR(N)=FRAC*ENQ2(NV1,N)
      ENET(L)=ENET(L)+EINCR(N)
4600 CONTINUE
C
C   NOW FOR Q21,Q12 LOOPS
C
      DO 5500 N=1,25
      WDELTA=WSCAN(L)-WAVQ21(NV1,N)
      DELTA=ABS(WDELTA)
      IF(DELTA.GT.RES) GO TO 5425
      FRAC=(RES-DELTA)/RES
      GO TO 5450
5425 FRAC=0.000
5450 EINCR(N)=FRAC*ENQ21(NV1,N)
      ENET(L)=ENET(L)+EINCR(N)
5500 CONTINUE
      DO 5600 N=1,25
      WDELTA=WSCAN(L)-WAVQ12(NV1,N)
      DELTA=ABS(WDELTA)
      IF(DELTA.GT.RES) GO TO 5525
      FRAC=(RES-DELTA)/RES
      GO TO 5550
5525 FRAC=0.000
5550 EINCR(N)=FRAC*ENQ12(NV1,N)
      ENET(L)=ENET(L)+EINCR(N)
5600 CONTINUE
C
C   NOW FOR R21,P12 LOOPS
C

```

```

DO 6500 N=1,25
WDELTA=WSCAN(L)-WAVR21(NV1,N)
DELTA=ABS(WDELTA)
IF (DELTA.GT.RES) GO TO 6425
FRAC=(RES-DELTA)/RES
GO TO 6450
6425 FRAC=0.000
6450 EINCR(N)=FRAC*ENR21(NV1,N)
ENET(L)=ENET(L)+EINCR(N)
6500 CONTINUE
DO 6600 N=1,25
WDELTA=WSCAN(L)-WAVP12(NV1,N)
DELTA=ABS(WDELTA)
IF (DELTA.GT.RES) GO TO 6525
FRAC=(RES-DELTA)/RES
GO TO 6550
6525 FRAC=0.000
6550 EINCR(N)=FRAC*ENP12(NV1,N)
ENET(L)=ENET(L)+EINCR(N)
6600 CONTINUE
C
6700 CONTINUE
C
C NOW WRITE DATA TO FILE
C
WRITE(23,7895) WSCAN(L),CHAR(9),ENET(L)
7895 FORMAT (F8.3,A1,F8.2)
C
C
IF (L.EQ.100) GO TO 7900
IF (L.EQ.200) GO TO 7900
IF (L.EQ.300) GO TO 7900
IF (L.EQ.400) GO TO 7900
IF (L.EQ.500) GO TO 7900
IF (L.EQ.600) GO TO 7900
IF (L.EQ.750) GO TO 7900
IF (L.EQ.1000) GO TO 7900
IF (L.EQ.1250) GO TO 7900
IF (L.EQ.1500) GO TO 7900
GO TO 8000
7900 WRITE (9,7950) L,NDATA
7950 FORMAT (I4,'/',I4,2X,'DATA POINTS')
8000 CONTINUE
WRITE (9,8100)
8100 FORMAT (/, 'SCANNING COMPLETE - POST-PROCESSING UNDERWAY',/)
C
C
CALL FILECR('DATA')
C
8200 CLOSE (UNIT=23)
8300 END
C
C
C This subroutine changes the File whose name is passed
C to the type and creator of a KALEIDAGRAPH text
C file. Created and modified by F. Frederick II and
C J. Amfahr.
C

```

```

SUBROUTINE FILECR( NAME )
C
character*(*) NAME
INTEGER*4 toolbox
CHARACTER*256 FILENAME
INTEGER PTR
PARAMETER (PTR=Z'C0000000')
C
include XP 20:FORTTRAN:INCLUDE FILES:file.inc .
include XP 20:FORTTRAN:INCLUDE FILES:params.inc
C
C change the file name to a PASCAL string
C
FILENAME = char(len(TRIM( NAME)))/TRIM(NAME )
C
C set the toolbox parameters to call PBGETFILEINFO
C
ionameptr = toolbox(PTR, FILENAME )
iocompletion = 0
iofdirindex = -1
iocompletion = 0
iohrefnum = 0
iofversnum = 0
C
C toolbox routine to get file info
C
CALL toolbox(PBGETFILEINFO, toolbox(PTR, params))
C
C Kaleidagraph text file type and creator
C
fdtype = 'TEXT'
fdcreator = 'QKPT'
C
C toolbox routine to set file info
C
CALL toolbox(PBSETFILEINFO, toolbox(PTR, params))
C
RETURN
END

```